

# Constraining the circumbinary disc tilt in the KH 15D system

Michael Poon<sup>1b</sup>,<sup>1,2</sup>★ J. J. Zanazzi<sup>1b</sup> and Wei Zhu<sup>1b</sup><sup>1,3</sup>

<sup>1</sup>Canadian Institute for Theoretical Astrophysics, University of Toronto, 60 St George Street, Toronto, ON S5 1A7, Canada

<sup>2</sup>Department of Astronomy and Astrophysics, University of Toronto, Toronto, ON M5S 3H4, Canada

<sup>3</sup>Department of Astronomy, Tsinghua University, Beijing 100084, China

Accepted 2021 February 24. Received 2021 February 12; in original form 2020 September 30

## ABSTRACT

KH 15D is a system that consists of a young, eccentric binary, and a circumbinary disc that obscures the binary as the disc precesses. We develop a self-consistent model that provides a reasonable fit to the photometric variability that was observed in the KH 15D system over the past 60 yr. Our model suggests that the circumbinary disc has an inner edge  $r_{\text{in}} \lesssim 1$  au, an outer edge  $r_{\text{out}} \sim$  a few au, and that the disc is misaligned relative to the stellar binary by  $\sim 5\text{--}16^\circ$ , with the inner edge more inclined than the outer edge. The difference between the inclinations (warp) and longitude of ascending nodes (twist) at the inner and outer edges of the disc are of order  $\sim 10$  and  $\sim 15^\circ$ , respectively. We also provide constraints on other properties of the disc, such as the precession period and surface density profile. Our work demonstrates the power of photometric data in constraining the physical properties of planet-forming circumbinary discs.

**Key words:** techniques: photometric – planets and satellites: formation – protoplanetary discs – binaries: spectroscopic – stars: individual: KH 15D.

## 1 INTRODUCTION

Our understanding of tilts within planet-forming circumbinary systems has undergone drastic changes within the past decade. Originally, the basic picture was quite simple: a circumbinary disc should always be observed to be aligned with the orbital plane of the binary. Even though simulations of turbulent molecular clouds found circumbinary discs frequently formed misaligned with the orbital plane of the binary (e.g. Bate, Bonnell & Bromm 2002; Bate 2012, 2018), viscous disc-warping torques were showed to damp the disc–binary inclination over time-scales much shorter than typical protoplanetary disc lifetimes (Foucart & Lai 2013, 2014). Most inclination constraints on protoplanetary (e.g. Andrews et al. 2010; Rosenfeld et al. 2012; Czekala et al. 2015, 2016; Ruíz-Rodríguez et al. 2019) and debris (e.g. Kennedy et al. 2012b) discs confirm this basic picture, finding alignment of the disc with the orbital plane of the binary to within a few degrees.

However, after the detection of a few highly inclined circumbinary discs (e.g. Kennedy et al. 2012a; Marino, Perez & Casassus 2015; Brinch et al. 2016; Czekala et al. 2017), it became clear not all circumbinary discs align rapidly. Motivated by these detections of highly inclined discs, the theoretical community found that when a circumbinary disc orbits an *eccentric* binary, the disc–binary inclination can grow under certain circumstances, evolving eventually to  $90^\circ$  (polar alignment; Aly et al. 2015; Martin & Lubow 2017; Zanazzi & Lai 2018). Additional inclined circumbinary discs orbiting eccentric binaries were discovered soon thereafter, such as HD 98800 (Kennedy et al. 2019), and AB Aurigae (Poblete et al. 2020). Recently, Czekala et al. (2019) showed circumbinary discs had

larger inclinations when orbiting binaries with higher eccentricities, further supporting the operation of this mechanism in circumbinary disc systems.

The alignment process itself was also shown to be non-trivial, with the disc itself occasionally breaking in the process. Early on, the disc was expected to remain nearly flat, due to the resonant propagation of bending waves across the disc (Papaloizou & Lin 1995; Lubow & Ogilvie 2000). Later hydrodynamical simulations found that the disc under some circumstances may break, with different disc annuli becoming highly misaligned with one another, due to strong differential nodal precession induced by the torque from the binary (e.g. Facchini, Lodato & Price 2013; Nixon, King & Price 2013). Numerous broken protoplanetary discs orbiting two binary stars have subsequently been found, including HD 142527 (Marino, Perez & Casassus 2015; Price et al. 2018) and GW Ori (Bi et al. 2020; Kraus et al. 2020).

The inclinations of detected circumbinary planets, in contrast, remain broadly consistent with formation in nearly aligned circumbinary discs. After the detection of a few dozen circumbinary planets (see Doyle & Deeg 2018; Welsh & Orosz 2018 for recent reviews), the inclinations within the circumbinary planet population are consistent with alignment to within  $\sim 4^\circ$  (Armstrong et al. 2014; Martin & Triaud 2014; Li, Holman & Tao 2016). However, highly misaligned circumbinary planets are physically allowed, because the inclined orbit has been shown to be long-term stable once a planet forms in the polar-aligned circumbinary disc (Doolin & Blundell 2011; Chen et al. 2019; Giuppone & Cuello 2019; Chen, Lubow & Martin 2020). New detection methods may detect polar-aligned circumbinary planets in the future (Zhang & Fabrycky 2019).

While a large number of systems now have constraints on mutual inclinations between the disc and the binary orbital planes, there remain few constraints on twists and warps within the circumbinary

★ E-mail: michaelkm.poon@mail.utoronto.ca

disc itself. This is because the methods used to constrain disc inclinations are not sensitive to the small misalignments within the disc. Gaseous protoplanetary disc inclinations are constrained via the orbital motion of the disc gas through the Doppler shift of emission lines (e.g. Facchini, Juhász & Lodato 2018; Price et al. 2018). Debris disc inclinations are constrained by the orientation of the disc implied by its continuum emission (e.g. Kennedy et al. 2012a, b).

A rare example of a circumbinary disc<sup>1</sup> system where photometric constraints exist is Kearns-Herbst 15D (KH 15D) (Kearns & Herbst 1998). KH 15D is a system with a highly unusual light curve, which exhibited dips by up to 5 mag. The morphology of the dipping behaviour changed over decade-long time-scales, but displayed periodicity over short 48-d time-scales. The complex light curve of this system is generally believed to be due to a circumbinary disc and a binary star, with some of the dips caused by the optically thick, precessing disc slowly and obscuring the orbital plane of the stellar binary (Chiang & Murray-Clay 2004; Winn et al. 2004, 2006; Capelo et al. 2012). Although much work has gone into understanding KH 15D, no work has attempted to provide quantitative constraints on the properties of the warped disc based on the photometric data.

In this work, we combine the spectroscopic and photometric data to constrain the properties of the circumbinary disc KH 15D. With recent data up to 2018 from Aronow et al. (2018) and García Soto et al. (2020), we improve the Winn et al. (2006) model to fit all photometric data since 1955. Our results are particularly exciting, as our fit nearly encompasses the full transit of the circumbinary disc of KH 15D. Section 2 extends the Winn et al. (2006) model to fit the light curve of the system, over the more than 60 yr duration the system was observed. Section 3 develops a dynamical model to constrain the circumbinary disc properties implied by the photometric constraints. Section 4 discusses the theoretical implications of our work, improvements which can be made to our model, and our model predictions that can be tested with future observations. Section 5 summarizes the conclusions of our work.

## 2 MODELLING THE LIGHT CURVE OF KH 15D

### 2.1 Photometric and radial velocity observations

We use radial velocity (RV) observations to constrain the orbit of the stellar binary and photometric data to constrain the geometry of the optically thick, precessing disc. We begin with a brief description of the RV and photometric data used in this work.

We use the RV measurements gathered by Hamilton et al. (2003) and Johnson et al. (2004), and because one of the stars is occulted by the disc when the RV measurements are taken, this is effectively a single-lined spectroscopic binary. As in Winn et al. (2006), we only use RV measurements gathered when the system flux is 90 per cent or greater than its mean out-of-occultation flux, because the Rossiter–McLaughlin effect (McLaughlin 1924; Rossiter 1924) leads to systematic errors as the stellar companion is occulted by the

<sup>1</sup>In this work, we use the terminology disc, rather than ring, to describe the object (likely) extending only to a few au around the KH 15D stellar binary. Although this runs counter to more traditional ideas of what a protoplanetary disc is within the planet-formation community, which has envisioned a disc as a gaseous object orbiting a young stellar object out to tens or hundreds of au, recent observations have detected more compact protoplanetary discs. Pegues et al. (2021) found the CO emission around the young M-dwarf FP Tau extended to  $\sim 4$ –8 au, while Francis & van der Marel (2020) resolved the size of the inner discs in a number of transition disc systems to lie near or within  $\sim 1$ –10 au.

disc.<sup>2</sup> This gives 12 RV measurements to aid in constraining the orbit of the binary.

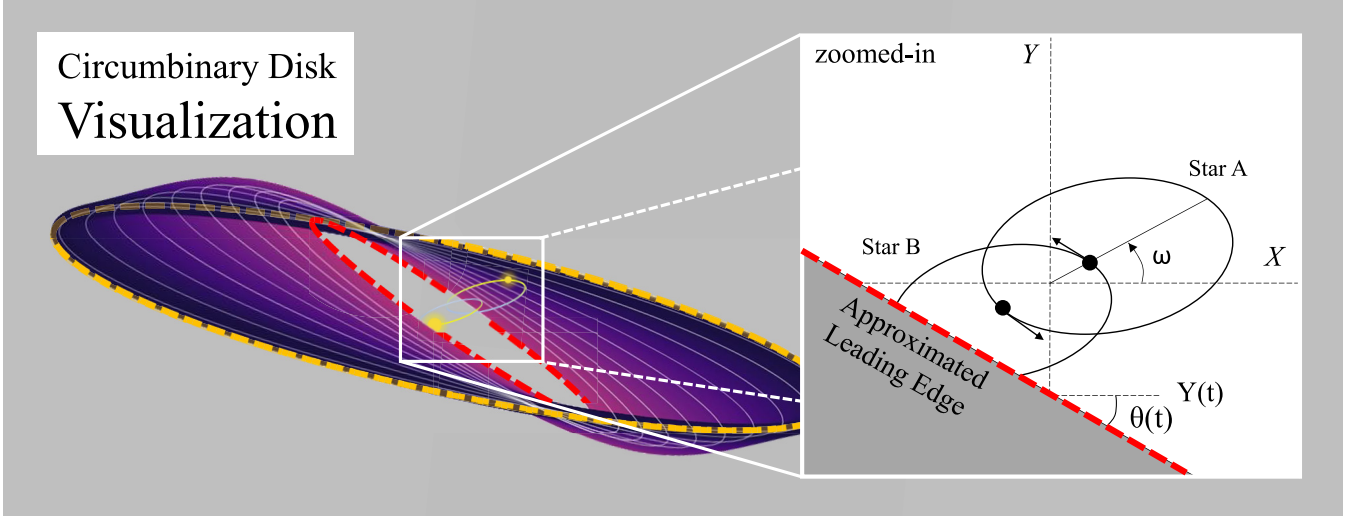
For the photometry, we use the tabulated data from Winn et al. (2006), Aronow et al. (2018), and García Soto et al. (2020). Details about the photometric observations can be found in these references, and we only provide a brief summary here. These catalogues include data from photographic plates from the 1950s to 1985 (Johnson & Winn 2004; Maffei, Ciprini & Tosti 2005), as well as observations using charge-coupled devices (CCDs) since 1995 (e.g. Hamilton et al. 2005; Capelo et al. 2012; Aronow et al. 2018; García Soto et al. 2020). No observations were known to be taken between 1985 and 1994. All photometric observations have been transformed into the standard Cousins *I*-band measurements. We bin the original data set (6241 points) into 2813 data points in order to reduce the amount of time needed for the photometric model computation. The uncertainties of all photometric measurements are re-scaled up by a factor of two, to allow for a model fit which gives a reduced  $\chi^2$  close to unity.

### 2.2 Previous models for KH 15D

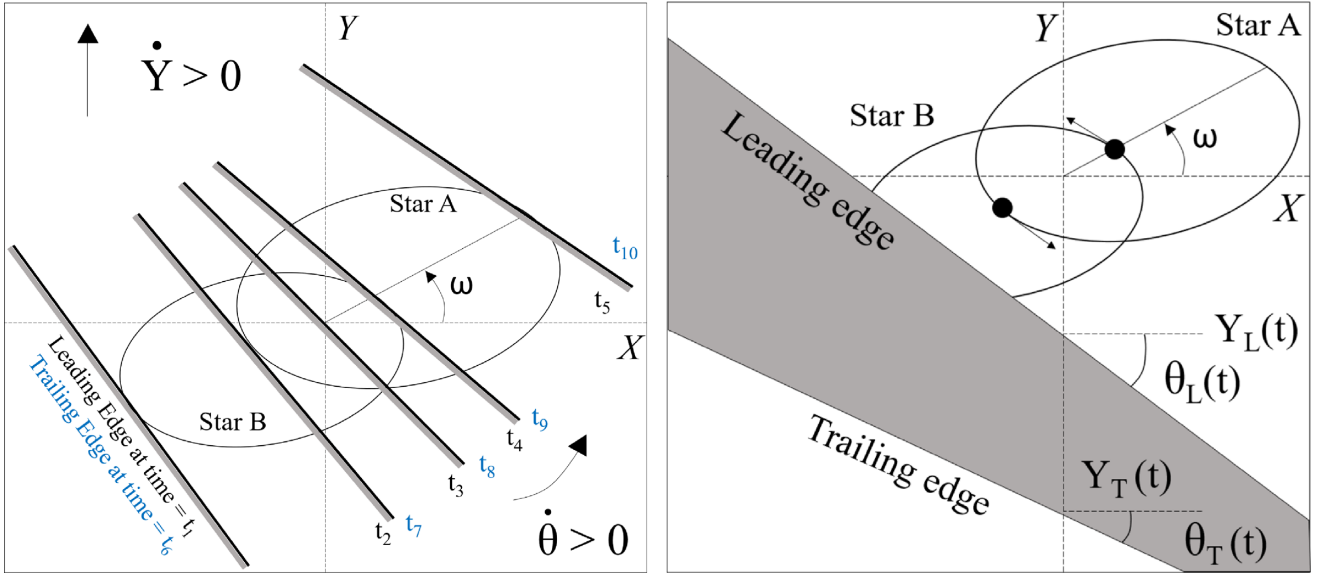
So far four models have been proposed to explain the photometric variation in the KH 15D system. The phenomenological model by Winn et al. (2004, 2006) approximates the leading edge of the disc as an infinitely long and optically thick screen, which occults the two stars as the screen moves across the orbit of the binary. Motivated by dynamics, Chiang & Murray-Clay (2004) treat the KH 15D disc as a warped disc with finite optical depth, and model the photometric variations by a disc precessing into and out of the line of sight of the observer. Silvia & Agol (2008) developed their model based on the model of Winn et al. (2006), but introduced more disc-related physics, such as the finite optical depth, curvature near the edge, and forward-scattering of starlight from the dust in the disc (which was parametrized as ‘haloes’ in the Winn et al. 2006 model). The fourth model is that of García Soto et al. (2020), who extended the Winn et al. (2006) model to include a trailing, as well as leading, edge. We choose to build our model based on Winn et al. (2006), because it allows us to remain agnostic about the detailed physics of the disc itself, while still accurately fitting the light curve of KH 15D. We review the Winn et al. (2006) model within this subsection.

Fig. 1 illustrates the physical motivation behind the Winn et al. (2006) model. A single ‘leading’ edge (red dashed line) slowly advances over the orbital plane of the binary, which approximates the inner or outer truncation radius of the disc slowly covering both stars as the disc is precessing around the binary. For data taken before 2005, it is reasonable to neglect the outer disc truncation radius (the ‘trailing’ edge, as marked by the yellow dashed curve). To model how quickly the leading edge advanced across the orbit of the binary, Winn et al. (2006) used the latest date when star B was still visible ( $t_4$ ), and the latest date when the orbit of star A was visible ( $t_5$ , see Fig. 2 left-hand panel), as free parameters in their model. In addition, not only was the angle the leading edge made with the *X*-axis of the observer allowed to vary, but it was also allowed to change at a constant rate, controlled by two free parameters  $\theta_1(t_4)$  and  $\dot{\theta}_L$ . The light from the binary was modelled with seven parameters, with the luminosity from star A (B) denoted by  $L_A$  ( $L_B$ ), the background light when the disc fully occults the binary by  $L_0$ , with the parameters  $\{\epsilon_1, \epsilon_2, \xi_1, \xi_2\}$  parametrizing

<sup>2</sup>We note that the Rossiter–McLaughlin effect is only important in this system, if the KH 15D disc edges are sharp, not diffuse.



**Figure 1.** The purple ellipses display a potential shape for the circumbinary disc of KH 15D. No assumption about the inclination between the innermost edge (red dashed curve), outermost edge (yellow dashed curve), or binary plane (centre yellow ellipses) are made while modelling the occultations of KH 15D. We note that our model also allows for the leading edge to be the outermost truncation radius of the disc, with the trailing edge as the innermost truncation radius of the disc. The zoomed-in inset diagram displays how the circumbinary disc geometry occults the binary of KH 15D. The inner or outer truncation radius of the disc slowly covers the orbital plane of the binary, as the disc precesses around the orbital angular momentum axis of the binary. We approximate the inner and outer disc edges as straight edges as the binary is occulted.



**Figure 2.** *Left-hand panel:* Definitions of orbital contact times. The leading (trailing) edge has contact times  $t_1$  to  $t_5$  ( $t_6$  to  $t_{10}$ ). All contact times denote when the leading or trailing edge lies tangent to the orbit of either star A or B, with the exception of  $t_3$  and  $t_6$ , which denote when the leading or trailing edges intersect the centre of mass of the binary. *Right-hand panel:* The definitions of quantities related to our model of the disc occulting the binary of KH 15D, which we model as an opaque screen bounded by two infinitely long, straight edges on both sides. The leading (trailing) edge is parametrized by its intersection with the  $Y$ -axis,  $Y_L$  ( $Y_T$ ), and the angle between the edge and the  $X$ -axis,  $\theta_L$  ( $\theta_T$ ). Our model allows for  $Y_L$ ,  $\theta_L$ ,  $Y_T$ , and  $\theta_T$  to evolve (linearly) with time. We emphasize our model makes no assumption on the underlying geometry of the disc occulting the binary of KH 15D.

the light emitted by haloes surrounding stars A and B. Specifically, the 1D brightness distribution from star  $i = A, B$  was taken to be

$$B_i(v) = \begin{cases} (\epsilon_1/\xi_1) \exp[(v+1)/\xi_1] & v \leq -1 \\ (\epsilon_1/\xi_1) + B_{*i}(v) & -1 < v < 1 \\ (\epsilon_2/\xi_2) \exp[-(v-1)/\xi_2] & v \geq 1 \end{cases}, \quad (1)$$

where  $B_{*i}$  is the 1D brightness distribution of star  $i$ , assuming a linear limb-darkening model:

$$B_{*i}(v) = 2I_i \sqrt{1-v^2} \left[ 1 - u \left( 1 - \frac{\pi}{4} \sqrt{1-v^2} \right) \right]. \quad (2)$$

Here,  $u = 0.65$  is the limb-darkening coefficient for both stars, and  $I_i$  is the reference intensity of star  $i$ . Letting  $y_{L,i}$  be the distance of the

lead edge from star  $i$ , and  $v_{L,i} = y_{L,i}/R_i$ , then the flux from star  $i$  is

$$F_{L,i} = \int_{v_{L,i}}^{\infty} B_i(v) dv, \quad (3)$$

with the total flux  $F = F_{L,A} + F_{L,B}$ . Physically, each ‘halo’ parametrizes forward-scattering of starlight by dust in the disc (Winn et al. 2006; Silvia & Agol 2008). The mass and radius for star A were taken to be  $M_A = 0.6 M_{\odot}$  and  $R_A = 1.3 R_{\odot}$ , while the ratios between the masses and radii of the two stars are  $M_B/M_A = 1.2$  and  $R_B/R_A = 1.05$ , respectively. The orbit of the binary is described by standard orbital parameters used to model RV data, with an orbital period  $P$ , eccentricity  $e$ , inclination  $I$ , longitude of pericentre  $\omega$ , time of pericentre passage  $T_p$ , and line-of-sight velocity  $\gamma$  (see e.g. Fulton et al. 2018 for details). The Cartesian coordinate system in the sky-projected reference plane of the observer ( $X, Y$ ) is chosen so the  $X$ -axis lies along the line of nodes (so  $\Omega = 0$ ).

The best-fitting model parameters for the KH 15D system was then calculated by minimizing (Winn et al. 2004, 2006)

$$\chi^2 = \sum_{j=1}^{N_F} \left( \frac{F_j - F_{O,j}}{\sigma_{F,j}} \right)^2 + \lambda \sum_{j=1}^{N_V} \left( \frac{V_j - V_{O,j}}{\sigma_{V,j}} \right)^2$$

$$\equiv \chi_{\text{phot}}^2 + \lambda \chi_{\text{RV}}^2, \quad (4)$$

where  $\chi_{\text{phot}}^2$  is the  $\chi^2$  of the photometry model alone,  $\chi_{\text{RV}}^2$  is the  $\chi^2$  metric of the modelled orbit of the binary in relation to the RV data (see Fulton et al. 2018 for details), and for a quantity  $X$ ,  $X_j$  denotes the model prediction at point  $j$ ,  $X_{O,j}$  denotes the observed value of  $X$  at  $j$ , while  $\sigma_{X,j}$  denotes the uncertainty of  $X_{O,j}$  at  $j$ . The parameter  $\lambda = 50$  was chosen to increase the importance of the RV model relative to that for the photometry, because the model constraining the orbit of the binary (a Keplerian orbit) is much more certain than the model describing the light curve of the binary (occulted by a precessing disc).

Because the screen advances in the positive vertical direction at a constant rate, an equivalent way of parametrizing the ascent of the screen are through where the screen intersects the  $Y$ -axis at the orbital contact time  $t_4$ , which we will denote by  $Y_L(t_4)$  (see Figs 1 and 2), and the rate of change in the  $Y$ -direction,  $\dot{Y}_L$ . Winn et al. (2006) choose  $t_4$  and  $t_5$  because of its tighter connections with observations ( $t_4$  and  $t_5$  denote changes in the light curve of KH 15D). When extending the Winn et al. (2006) model, we will also primarily refer to orbital contact times to parametrize the advance of the screen across the orbit of the binary (Fig. 2), but also frequently refer to  $Y_L$  and  $\dot{Y}_L$  as well.

### 2.3 Our model for the KH 15D system

Our photometric model builds off of Winn et al. (2006), and seeks to fit the light curve of KH 15D from 1955–2018 with minimal modifications (smallest number of additional parameters to describe the trailing edge, in relation to the leading edge). After 2012, the trailing edge started to uncover star B, due to the other (inner or outer) truncation radius of the disc of KH 15D precessing over the binary orbit with respect to the line of sight of the observer (see Fig. 1). The simplest extension is to include an additional trailing edge in the modelling (denoted by subscript T), which lags in position behind the leading edge (with subscript L), which intersects the  $Y$ -axis at a location  $Y_T(t)$  (see Fig. 2). This trailing edge also introduces five new orbital contact times as the edge crosses the orbit of the binary:  $t_6, t_7, t_8, t_9, t_{10}$  (see Fig. 2 for illustration). Assuming  $\theta_L = \theta_T$  and  $\dot{Y}_L = \dot{Y}_T$ , the previous 1-edge semi-infinite sheet becomes a 2-edge

**Table 1.** Definitions of model parameters.

Free parameter	Description
$P$	Orbital period
$e$	Orbital eccentricity
$I$	Inclination of orbital plane
$\omega$	Argument of pericentre
$T_p$	Time of periastris passage
$L_B/L_A$	Luminosity of star B relative to star A
$\epsilon_1$	Fractional flux of stellar halo <sup>a</sup>
$\epsilon_2$	Fractional flux of stellar halo <sup>b</sup>
$\xi_1$	Exponential scale factor of stellar halo <sup>a</sup>
$\xi_2$	Exponential scale factor of stellar halo <sup>b</sup>
$t_3$	Third orbital contact time <sup>c</sup>
$t_5$	Fifth orbital contact time <sup>c</sup>
$t_6$	Sixth orbital contact time <sup>c</sup>
$\theta_L(t_3)$	Angle between $x$ -axis and leading edge at $t = t_3$
$\theta_T(t_3)$	Angle between $x$ -axis and trailing edge at $t = t_3$
$\dot{\theta}_L$	Rotation rate of leading edge when $t < t_3$
$\dot{\theta}_L$	Rotation rate of leading edge when $t > t_3$
$\dot{\theta}_T$	Rotation rate of trailing edge

<sup>a</sup>In the direction the leading edge approaches the star.

<sup>b</sup>In the direction the leading edge travels beyond the star.

<sup>c</sup>Defined in Fig. 2.

thin rectangular sheet of constant width, which is infinite along its length. García Soto et al. (2020) assumed this for their light curve model, and neatly fit CCD photometry from 1995 and onwards. However, because this fit does not match the light curve data prior to 1995 (fit not shown here or in García Soto et al. 2020), further modifications are needed to the Winn et al. (2006) and García Soto et al. (2020) model.

Through much experimentation, we found the following set of additions to the Winn et al. (2006) model that let us fit the 60+ yr light curve. The connection of these additions with a warped disc driven into precession by an eccentric binary will be made clear in the following section.

(i) We let the leading and trailing edges have different angles ( $\theta_L[t] \neq \theta_T[t]$ , see Fig. 2).

(ii) We let each edge linearly evolve in time independently ( $\dot{\theta}_L[t] \neq \dot{\theta}_T[t]$ ).

(iii) Parametrize  $\dot{\theta}_L$  by two constant, piecewise rates in time:  $\dot{\theta}_L(t) = \dot{\theta}_{L1}$  when  $t < t_3$ , and  $\dot{\theta}_L(t) = \dot{\theta}_{L2}$  when  $t > t_3$ . We keep  $\dot{\theta}_T(t) = \text{constant}$  as a single parameter. Because we make the leading edge symmetric about  $t_3$ , we fit for the times  $\{t_3, t_5\}$  in our MCMC model to constrain  $Y_L(t_3)$  and  $\dot{Y}_L$ , rather than  $\{t_4, t_5\}$  as in Winn et al. (2006).

(iv) Let the width of the screen change over time ( $\dot{Y}_L \neq \dot{Y}_T$ ), but keep both rates  $\dot{Y}_L$  and  $\dot{Y}_T$  constant with time.

(v) Prescribe the rate of ascent of the trailing edge in relation to the rate of ascent of the leading edge. Specifically, we take  $\dot{Y}_T = \alpha \dot{Y}_L$  for  $\alpha = 0.1, 0.3, 0.5, 2.0, 3.0, 10.0$ . We also experimented with letting  $\dot{Y}_T$  be a free parameter (fitting for the contact times  $\{t_6, t_7\}$ ), and found these fits gave  $\dot{Y}_T \approx \dot{Y}_L$ , but the MCMC did not always converge. We choose this parametrization to make sure the other model parameters are well determined.

We further simplify the Winn model by analytically solving for  $L_A$  and  $\gamma$  with respect to the rest of the parameters, since they are constant shifts to the photometric and RV models, respectively. This reduces the number of free parameters by 2. For reference, we display each model parameter and its definition in Table 1.



To calculate the flux from the KH 15D system, we simply add the flux from stellar light emitted exterior to the trailing edge, to that emitted exterior to the leading edge. In more detail, letting  $y_{T,i}$  be the distance of the trailing edge from star  $i$ , with  $v_{T,i} = y_{T,i}/R_i$ , star  $i$  emits the flux

$$F_{T,i} = \int_{-\infty}^{v_{T,i}} B_i(v) dv \quad (5)$$

exterior to the trailing edge, giving the total flux  $F = F_{L,A} + F_{L,B} + F_{T,A} + F_{T,B}$ . We neglect the intersection between the leading and trailing edges in the flux calculation, because this intersection occurs far from the orbit of the binary.

For our RV model, we follow equations 2 and 3 from section 2.1 of Fulton et al. (2018). To optimize the model parameters, we use a Python-implemented Markov chain Monte Carlo (MCMC) package EMCEE by Foreman-Mackey et al. (2013). We use the same  $\chi^2$  statistic as in equation (4).

Preliminary tests find the background light in the KH 15D system to be  $L_0 \approx 0$ , so we remove  $L_0$  from our model parameters. This is expected if  $L_0$  is from forward scattering of the stars' light around the trailing edge of the disc (Silvia & Agol 2008), rather than the finite optical depth of the disc itself (Chiang & Murray-Clay 2004), because forward scattering of stellar light around both screen edges is included in our model. Our final model has 18 parameters (see Table 1), which we run for 20000 steps with 36 walkers. Running the final model for each  $\alpha$ , we come to the following results: each MCMC converged except for  $\alpha = 10.0$ , with only  $\alpha = 0.3, 0.5$  producing reasonable-looking light curves. Model parameters for  $\alpha = 0.1, 0.3, 2.0, 3.0$  are reported in Table A1. We highlight  $\alpha = 0.5$  as the best fit with parameters in Table 2, and display corner plots of the posteriors in Fig. B1. Because no stellar eclipses have been detected in the KH 15D light curve (only the disc–binary occultations), we fix the binary inclination to be  $I \geq 91^\circ$  in our MCMC analysis, so the system is not perfectly edge-on.

Our fit for the entire light curve of KH 15D is displayed in Fig. 3. Our model does a good job in describing both the maximum and minimum fluxes from KH 15D, which change with time. As expected, the orbital contact times  $t_i$  denote when the light curve of the system changes its morphology. The gradual change of maximum/minimum flux around  $t_i$  values is due to the haloes around each star: for point source stars occulted by a razor-thin opaque edge, the photometric model predicts almost discontinuous changes in light curve morphologies around  $t_i$  values.

Figs 4 and 5 show the photometric model and data folded over the binary orbital period, which is comparable to fig. 12 in Winn et al. (2006). Again, we see our model does a good job at modelling changes in the light curve of KH 15D, with orbital contact times (see Table 2 for values) delineating morphology changes as one or both stars becomes occulted or revealed by an edge. Examining the data from 2013–2014 and 2015–2016, the large scatter makes it seem unlikely that any (simple) model could provide an accurate fit to the observed light curve. In addition, we do not remove any outliers (compare 1998–1999 panel in figs 4–12 in Winn et al. 2006). An interesting feature occurs around 2010, when the egress is poorly fit (for all values of  $\alpha$ ). This could be related to the clumpiness/transparency near the edges of the disc as discussed in García Soto et al. (2020), where the assumption of sharp edges breaks down.

**Table 2.** Model fits to photometric and RV data for the KH 15D system, taking  $\alpha = 0.5$ . Orbital parameters  $\{P, e, I, \omega, T_p\}$  are constrained using photometry and RV data, while the other parameters are constrained using photometry alone.

Parameter	Our fit
$P$ (d)	$48.3777^{+0.0002}_{-0.0002}$
$e$	$0.5784^{+0.0009}_{-0.0009}$
$I$ (deg)	$91.001^{+0.002}_{-0.001}$
$\omega$ (deg)	$11.80^{+0.06}_{-0.06}$
$T_p$ (JD) – 2452 350	$4.18^{+0.01}_{-0.02}$
$L_B/L_A$	$1.65^{+0.01}_{-0.01}$
$\epsilon_1$	$0.0436^{+0.0006}_{-0.0006}$
$\epsilon_2$	$0.0591^{+0.0008}_{-0.0008}$
$\xi_1$	$1.53^{+0.03}_{-0.03}$
$\xi_2$	$2.86^{+0.03}_{-0.03}$
$t_3$	$1992.68^{+0.05}_{-0.05}$
$t_5$	$2007.95^{+0.01}_{-0.01}$
$t_6$	$2013.57^{+0.03}_{-0.03}$
$\theta_L(t_3)$ (deg)	$-16.0^{+0.2}_{-0.2}$
$\theta_T(t_3)$ (deg)	$-5.3^{+0.2}_{-0.2}$
$\dot{\theta}_{L1}$ (rad yr $^{-1}$ )	$0.0077^{+0.0002}_{-0.0002}$
$\dot{\theta}_{L2}$ (rad yr $^{-1}$ )	$0.0033^{+0.0001}_{-0.0001}$
$\dot{\theta}_T$ (rad yr $^{-1}$ )	$-0.0006^{+0.0001}_{-0.0002}$
$\chi^2_{\text{phot}}$	13 325
$\chi^2_{\text{RV}}$	13
Reduced $\chi^2$	1.36
$t_1$	$1972.9 \pm 0.2^a$
$t_2$	$1987.00 \pm 0.01^a$
$t_4$	$1996.8 \pm 0.1^a$
$t_7$	$2020.8 \pm 0.1^a$
$t_8$	$2024.95 \pm 0.01^a$
$t_9$	$2028.6 \pm 0.1^a$
$t_{10}$	$2041.0 \pm 0.5^a$
$Y_T(t_3)$ (au)	$-0.05903^b$
$Y_L(t_6)$ (au)	$0.07642^b$
$Y_T(t_6)$ (au)	$-0.02082^b$
$\dot{Y}_L(t_6)$ (au yr $^{-1}$ )	$0.003658^b$
$\dot{Y}_T(t_6)$ (au yr $^{-1}$ )	$0.001829^b$

<sup>a</sup>Predicted by the free parameters.

<sup>b</sup>Best-fitting value, we do not calculate the errors implied by the  $t_i$  measurements.

### 3 A DYNAMICAL MODEL FOR THE DISC OF KH 15D

The previous section showed that in order for the Winn et al. (2006) model to fit the entire more than 60 yr light curve of KH 15D, a number of modifications to this original model must be made. In this section, we illustrate how these modifications are motivated by the dynamics of a warped disc, driven into precession around an eccentric binary. In doing so, we will show that the disc orientation, warp, radial extent, and even surface density profile may be constrained by photometry alone.

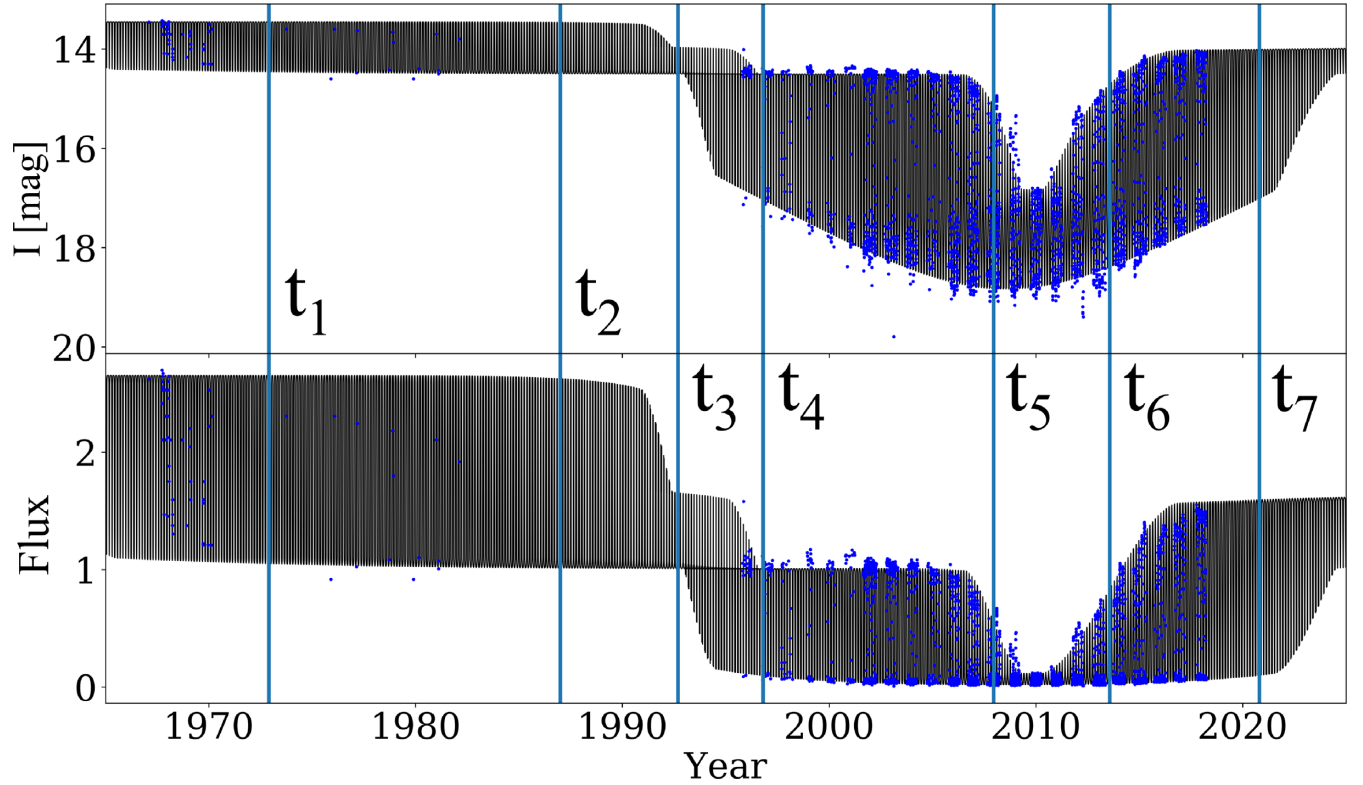


**Figure 3.** Light curve of KH 15D from 1965 to present, displaying the complex change in variability seen with time. The observed light curve in *I*-band magnitude is shown in the upper panel, and the light curve after the normalization to the flux of star A is shown in the lower panel. Blue points are photometry from Aronow et al. (2018) and García Soto et al. (2020), while the thin black line displays our photometric model fit (see Table 2 for parameter values). Vertical cyan lines denote the orbital contact times  $t_i$  indicated, where the leading or trailing edge of the screen (e.g. circumbinary disc, see Fig. 1) hits a different portion of the binary orbit (see Fig. 2 for definitions). Our model does well in reproducing the KH 15D light curve variability over the length of time the system is observed.

### 3.1 Model for a precessing, warped circumbinary disc orbiting KH 15D

For the disc around KH 15D to coherently precess over its lifetime, internal forces within the disc must keep neighbouring disc annuli nearly aligned with one another, otherwise differential nodal precession from the gravitational influence of the binary will disrupt and ‘break’ the disc (e.g. Larwood & Papaloizou 1997; Facchini, Lodato & Price 2013; Nixon, King & Price 2013; Martin & Lubow 2018). When these internal torques are much stronger than the external torque on the disc from the binary, the disc behaves as a rigid body, coherently precessing about the orbital angular momentum axis of the binary (e.g. Martin & Lubow 2017; Moody, Shi & Stone 2019; Smallwood et al. 2019). To model the dynamical evolution of the disc, we will assume the disc behaves approximately like a rigid plate, treating the disc as a secondary whose mass is distributed between radii  $r_L$  and  $r_T$ .

However, before we introduce our model for an extended disc, we discuss the dynamics of a test particle on a circular orbit (which we will refer to as a ring), driven into precession by the torque from the binary. Many authors have shown the orbital angular momentum unit vector of the ring  $\hat{l}_r$  is driven into precession and nutation about either the orbital angular momentum unit vector of the binary  $\hat{l}$ , or eccentricity vector of the binary  $\mathbf{e}$  (vector in pericentre direction with magnitude  $e$ ). The dynamical evolution of the ring depends sensitively on the initial orientation of  $\hat{l}_r$  with respect to  $\hat{l}$  and  $\mathbf{e}$ , as well as the magnitude of the eccentricity of the binary  $e$ . To calculate the evolution of  $\hat{l}_r$  about  $\hat{l}$  and  $\mathbf{e}$ , we adopt the formalism

of Farago & Laskar (2010), who calculated the secular evolution of a ring about a massive binary with an eccentric orbit, after expanding the Hamiltonian of the binary to leading order in  $r/a$  (where  $r$  is the semimajor axis of the test particle), and averaging over the mean motions of the test particle and the binary. It was found the characteristic precession and nutation frequency of  $\hat{l}_r$  about the binary was given by (denoted by  $\alpha$  in Farago & Laskar 2010)

$$\nu = \frac{3\mu}{4M_t} \left( \frac{GM_t}{a^3} \right)^{1/2} \left( \frac{a}{r} \right)^{7/2}, \quad (6)$$

where  $M_t = M_A + M_B$  is the total mass of the binary, while  $\mu = M_A M_B / M_t$  is the reduced mass of the binary.

After calculating the evolution of a (circular) test particle  $\hat{l}_r$  vector about  $\hat{l}$  and  $\mathbf{e}$  using Farago & Laskar (2010), we then translate the evolution of  $\hat{l}_r$  into the inclination of the test particle  $I_r$  and longitude of ascending node  $\Omega_r$ , in the frame where  $\hat{z} = \hat{l}$  and the line of nodes points in the direction of  $\mathbf{e}$ . Because the orientation of the binary orbit in the reference frame of a distant observer is described by the orbital elements  $\{a, e, \omega, I, \Omega\}$ , the position of the ring in the frame of the observer is

$$\begin{pmatrix} x \\ y \\ z \end{pmatrix}_{r, \text{obs}} = R_Z(\Omega) R_X(I) R_Z(\omega) R_Z(\Omega_r) R_X(I_r) \begin{pmatrix} x_r \\ y_r \\ 0 \end{pmatrix}, \quad (7)$$

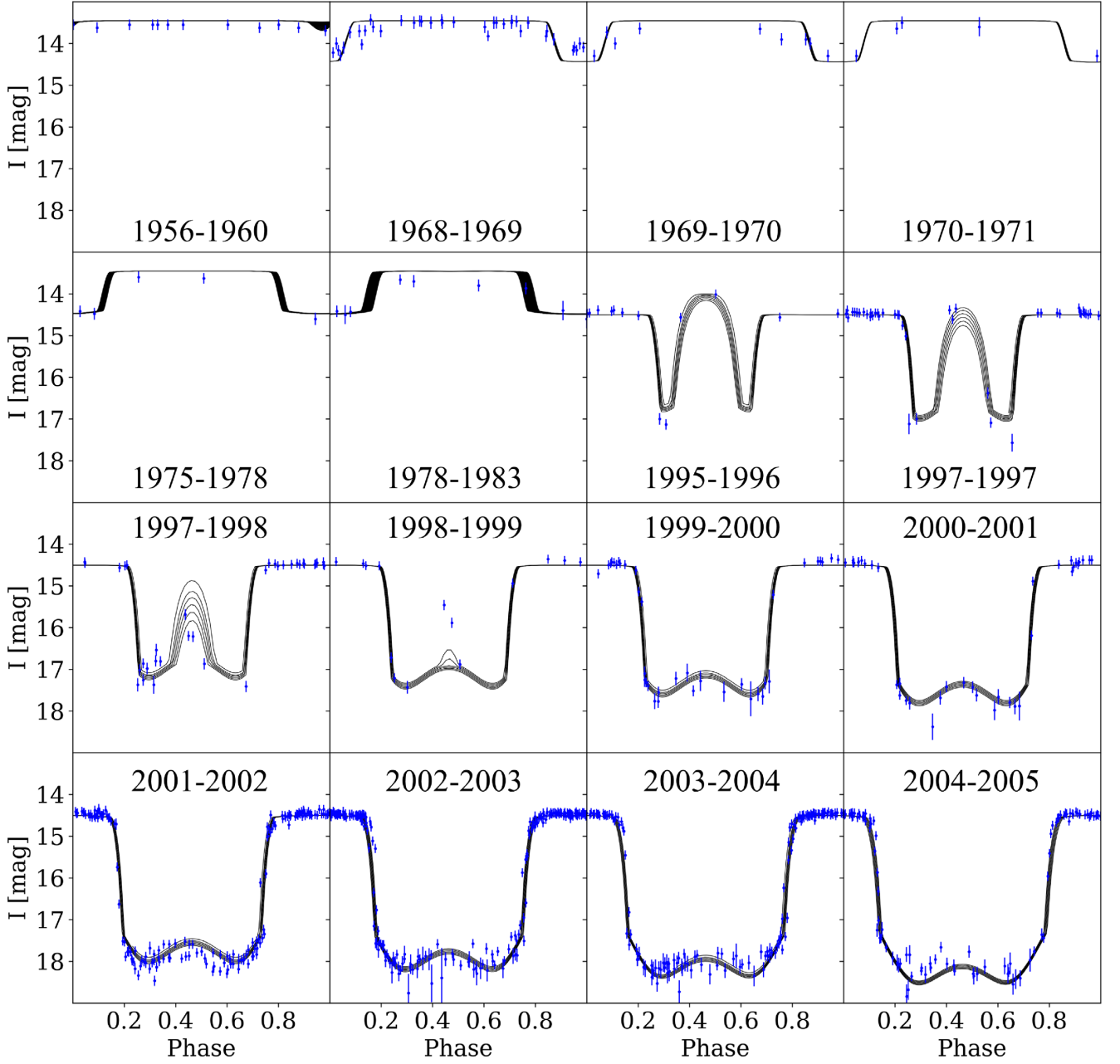


**Figure 4.** Data (blue points) and fitted model (black lines) displayed in Fig. 3, folded over the binary orbital period, prior to the year 2005. The timespan over which the data and model are folded over is displayed in each figure. Our model reproduces the changing morphology of the light curve of KH 15D well.

where  $(x_r, y_r) = r(\cos \varphi, \sin \varphi)$  parametrizes the  $(X, Y)$  coordinates of the ring in the frame where  $\hat{z} = \hat{l}$ , and  $R_X[\beta]$  ( $R_Z[\gamma]$ ) denote rotations along the  $X$  ( $Z$ )-axis by angles  $\beta$  ( $\gamma$ ). As in Winn et al. (2006), we choose the reference plane of the observer so the  $X$ -axis points along the binary line of nodes (so  $\Omega = 0$ ). Also, because our MCMC model highly favours a nearly edge-on orbit (Table 2), we assume  $i \simeq 90^\circ$  for simplicity for the rest of this section. All other orbital parameters are taken as their most likely values from Table 2.

To connect with a model for a disc occulting the binary of KH 15D, we approximate the inner and outer edges of the disc as two rings with different orbital elements  $\{r_k, I_k, \Omega_k\}$ , with  $k = L, T$  for the leading and trailing edges of the disc, respectively. Although each ring has a different  $r_k$ , we assume the rings precess about  $\hat{l}$  with the same global disc precession frequency  $\nu_d$ .

To connect the geometry of a disc occulting the binary of KH 15D with the edges of the light curve model in Section 2, we approximate an occulting ring by a line drawn tangent to the ring at the location where the ring intersects the  $X$ -axis of the system (see Fig. 6). The angle between the tangent line and  $X$ -axis  $\theta_k$ , as well as the  $Y$ -intercept  $Y_k$ , of ring  $k$  are then given by

$$\theta_k [I_k(t), \Omega_k(t)] = \tan^{-1} \left[ \frac{\tan I_k}{\sin(\omega + \Omega_k)} \right], \quad (8)$$

$$Y_k [I_k(t), \Omega_k(t)] = -\frac{r_k \tan I_k}{\tan(\omega + \Omega_k)}. \quad (9)$$

A successful model of the circumbinary disc of KH 15D would give values for  $\theta_k$  and  $Y_k$  which match the MCMC fits for  $\theta_L$ ,  $\theta_T$ ,  $Y_L$ , and  $Y_T$ , from Table 2.

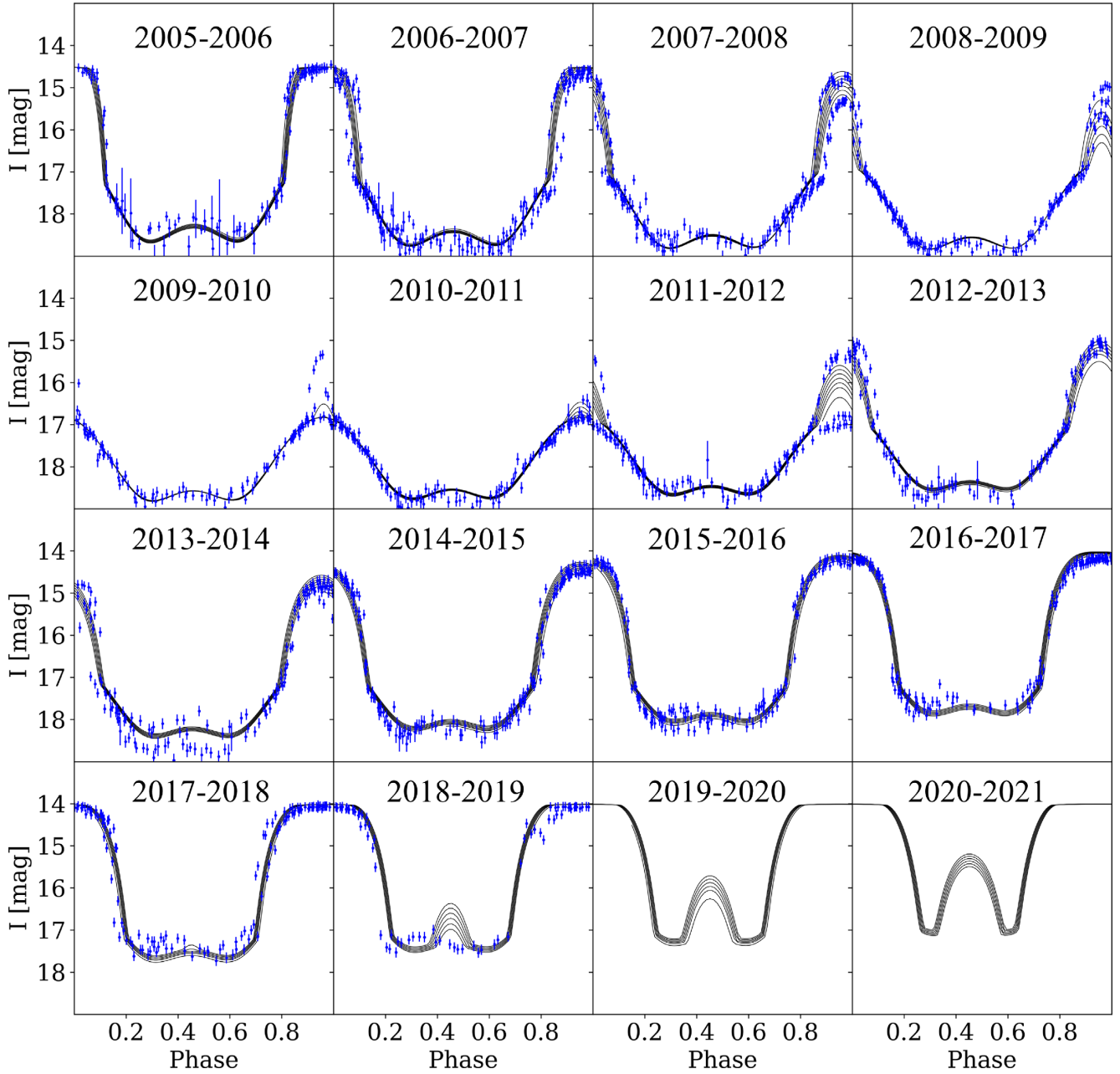


**Figure 5.** Same as Fig. 4, except for data and model fits after the year 2005. We also display model predictions for the years 2019–2021.

### 3.2 Estimates of disc properties from model fits

Before presenting an example warped disc geometry that matches the light curve model fit, we discuss how the warped disc geometry can be constrained by the MCMC fits of Section 2.3. To do this, we simplify equations (8) and (9), and derive order-of-magnitude estimates for all disc quantities. Because the pericentre direction of the binary is nearly perpendicular to the observer ( $\omega \ll 1$ ), the disc annuli longitude of ascending nodes satisfy  $\Omega_k \approx \pi/2$  during transit. The disc inclination is also nearly aligned with the orbital plane of the binary ( $|I_k| \ll 1$ ). Also, because the binary pericentre direction is nearly perpendicular to the observer, the inclination nutations should be near a local minimum (e.g. Farago & Laskar 2010; Zanazzi & Lai 2018), so  $\dot{I}_k \approx 0$ . The nodal regression rate of the rings should be of order  $\dot{\Omega}_k \approx -\nu_k$ , where  $\nu_k$  is the nearly constant nodal precession

rate of ring  $k$ . Defining  $\delta\Omega_k \equiv \Omega_k - \pi/2$ , and assuming  $|\omega|$ ,  $|I_k|$ , and  $|\delta\Omega_k| \ll 1$ , equations (8) and (9) can be shown to reduce to

$$\theta_k \approx I_k \quad (10)$$

$$\dot{\theta}_k \approx -(\omega + \delta\Omega_k)I_k\nu_k, \quad (11)$$

$$Y_k \approx r_k I_k (\omega + \delta\Omega_k), \quad (12)$$

$$\dot{Y}_k \approx -r_k I_k \nu_k. \quad (13)$$

From this, we see the increase of  $Y_L$  and  $Y_T$  is primarily due to nodal regression from the rings. The evolution of  $\theta_L$  and  $\theta_T$  is primarily due to the curvature of the ring, as it nodally precesses in front of the orbit of the binary (see Silvia & Agol 2008 for further discussion). Most



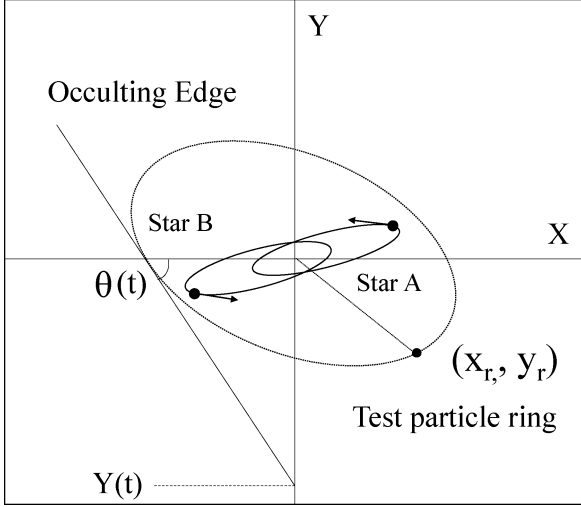


**Figure 6.** Our interpretation for the leading/trailing edges of the opaque screen in our photometry model. The leading/trailing edges of the screen are from the inner or outer disc truncation radii. The occulting disc edge is approximated by a straight line, drawn tangent to the intersection of the ring with the X-axis of the coordinate system. The  $\theta = \theta_k$  and  $Y = Y_k$  values of the leading/trailing edge are defined similarly as in Fig. 2. Because the binary is nearly edge-on, the straight-line approximation is excellent.

interestingly, the MCMC constraints on  $\theta_L$  and  $\theta_T$  directly translate to constraints on the ring inclinations  $I_L$  and  $I_T$ .

Assuming the disc precesses rigidly ( $\nu_L \approx \nu_T$ ), one can then constrain the disc radial extent. Equation (13) leads to

$$\frac{r_L}{r_T} \approx \frac{\theta_T}{\theta_L} \frac{\dot{Y}_L}{\dot{Y}_T} = 0.63 \left( \frac{\theta_T}{-5^\circ} \right) \left( \frac{-16^\circ}{\theta_L} \right) \left( \frac{0.5}{\alpha} \right). \quad (14)$$

Because the values of  $\alpha$  which fit the data are of order unity ( $0.3 \lesssim \alpha \lesssim 1$ ), we can be confident that the leading edge of the screen occulting the binary of KH 15D is the disc inner truncation radius, while the trailing edge is the outer truncation radius ( $r_L \lesssim r_T$ ).

Moreover, because  $\dot{\theta}_k$ ,  $Y_k$ , and  $\dot{Y}_k$  are all known, one can get unique solutions for  $r_k$ ,  $\delta\Omega_k$ , and  $\nu_k$ . Starting with  $\nu_k$ , equations (11)–(13) can be re-arranged to give

$$\nu_k \approx \left( \frac{\dot{\theta}_k \dot{Y}_k}{Y_k} \right)^{1/2}. \quad (15)$$

Evaluating estimate (15) at  $t = t_4$ , we find  $\nu_L \sim 0.013 \text{ yr}^{-1}$  and  $\nu_T \sim 0.0073 \text{ yr}^{-1}$ , which are consistent with one another within a factor of a few. Similarly, equation (13) can be solved for  $r_k$

$$r_k \approx -\frac{1}{\dot{\theta}_k} \left( \frac{Y_k \dot{Y}_k}{\dot{\theta}_k} \right)^{1/2}, \quad (16)$$

which gives  $r_L \sim 1.0 \text{ au}$  and  $r_T \sim 4.6 \text{ au}$  at  $t = t_4$  for our model. Last, either equation (11) or (12) can be solved for  $\delta\Omega_k$ .

Although these disc parameter estimates are far from unique, they provide constraints on the properties of the circumbinary disc within the KH 15D system. We can strongly conclude the disc–binary mutual inclination  $I_{\text{KH15D}}$  in the KH 15D system lies in the range  $5^\circ \lesssim I_{\text{KH15D}} \lesssim 16^\circ$ , with the disc inner edge more highly inclined than the outer edge (because  $I_L \gtrsim I_T$ ). The leading edge of the opaque screen crossing the binary orbit is from the disc inner edge, which is located at a radius  $r_L \lesssim 1 \text{ au}$ , while the trailing outer disc edge is located at  $r_T \sim \text{few au}$ .

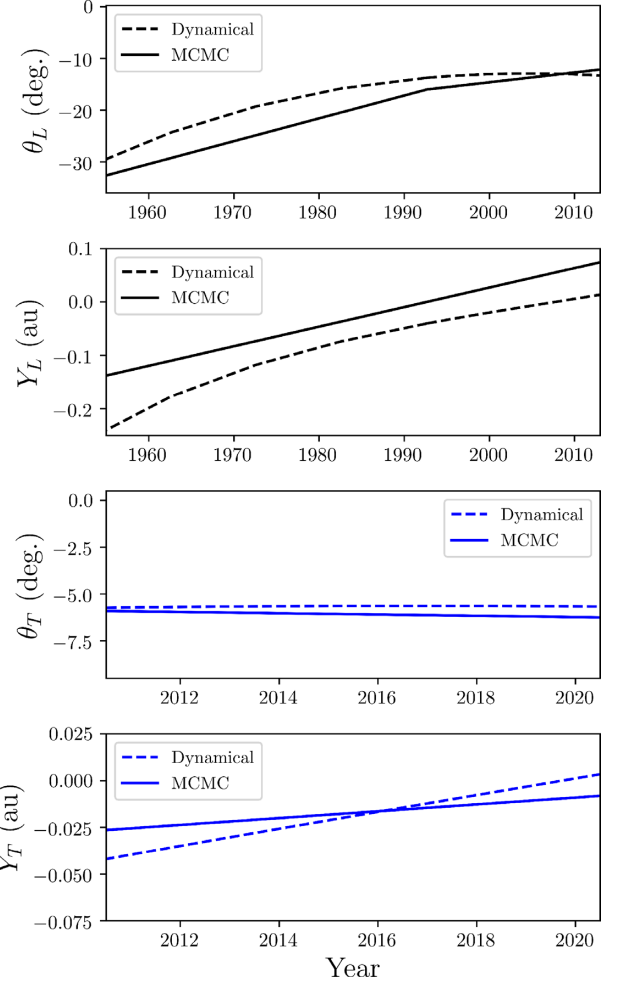


**Figure 7.** Comparing our dynamical warped disc model (Table 4) with the MCMC fits from our phenomenological photometry model (Table 2). Although agreement between the two models can be improved, the warped disc reproduces the main features of the photometry model.

### 3.3 Example warped disc which matches model fits

As we saw in the previous section, for a unique match to the phenomenological parameters  $\{\theta_k, \dot{\theta}_k, Y_k, \dot{Y}_k\}$  to a precessing, inclined ring annulus, we require the ring parameters  $\{r_k, I_k, \Omega_k, \nu_k\}$ . However, for a protoplanetary disc to exist over many dynamical times, it must precess rigidly ( $\nu_L = \nu_T$ ), decreasing the number of free parameters in one ring. Therefore, our dynamical model is overdetermined by our phenomenological model. To get accurate constraints on the warped disc itself using photometry, a light-curve model must be developed whose free parameters are directly related to the warped disc properties (disc inclination, warp, twist, precession frequency, etc.), rather than indirectly through a phenomenological model. The goal of this section is not to provide stringent constraints on the disc itself, but to present an example warped disc which gives gross light-curve features consistent with the MCMC light-curve fits.

Motivated by the estimated leading and trailing estimates in the previous subsection, we experiment with the warped disc orbital parameters and global precession frequency, to find a disc whose properties match the MCMC fitted parameters. Table 4 presents example model parameters for a dynamically evolving, warped disc whose features are compatible with the light-curve fits, with Fig. 7 displaying  $\theta_k(t)$  and  $Y_k(t)$  for both (dynamical and MCMC) models

over the duration of time the leading and trailing occultations have been observed. The dynamical model and MCMC fits match one another within a factor of a few, heavily reinforcing the idea that the light curve of KH 15D is caused by a warped, relatively narrow, precessing disc, occulting the starlight of the eccentric binary. In particular, we see the behaviour of the dynamical model matches the  $\theta_L(t)$  light-curve fit, reproducing the decrease in  $\dot{\theta}_L$  before and after the year  $t = t_3 \simeq 1993$ .

Complimentary constraints on the disc of KH 15D have come recently from the double-peaked line profile of neutral oxygen emission, assuming the [O I]  $\lambda 6300$  emission originates from the surface of the gaseous circumbinary disc of KH 15D (Fang et al. 2019). This line profile was used to constrain the disc radial extent, as well as the disc surface density profile. Fang et al. (2019) found an inner disc radius of  $r_{in} \approx 0.57$  au, an outer radius  $r_{out} \approx 5.2$  au, and surface density profile  $\Sigma \propto r^{-2.9}$ . The inner and outer radii are roughly consistent with our  $r_L = r_{in}$  and  $r_T = r_{out}$  values constrained by our crude dynamical fit to the photometry of KH 15D (Table 4). We note that the outer edge of a protoplanetary disc gas and dust radius may differ, due to radial drift of the dust (e.g. Weidenschilling 1977; Takeuchi & Lin 2002; Birnstiel & Andrews 2014; Powell, Murray-Clay & Schlichting 2017; Rosotti et al. 2019). Indeed, molecular line and continuum emission have been shown to extend to different radii around young stellar objects (e.g. Panić et al. 2009; Andrews et al. 2012; de Gregorio-Monsalvo et al. 2013; Ansdell et al. 2018; Facchini et al. 2019), showing gas and dust in protoplanetary discs often extend out to different radii (sometimes differing by as much as a factor of  $\sim 3$ ). The dynamics of dust in a precessing circumbinary disc can also be non-trivial (Poblete, Cuello & Cuadra 2019; Aly & Lodato 2020).

Our warped disc model can also constrain the disc surface density profile  $\Sigma \propto r^p$ , because the distribution of mass within the disc affects the torque exerted on the disc by the binary, modifying the disc precession frequency  $\nu_d$ . Assuming a nearly-flat disc which is driven into rigid-body precession about the binary,  $\nu_d$  can be shown to be (e.g. Lodato & Facchini 2013; Foucart & Lai 2014; Lubow & Martin 2018; Zanazzi & Lai 2018).

$$\nu_d = \frac{3}{4} \left( \frac{5/2 + p}{1 - p} \right) \left[ \frac{1 - (r_{out}/r_{in})^{p-1}}{(r_{out}/r_{in})^{5/2+p} - 1} \right] \frac{\mu}{M_t} \left( \frac{a}{r_{in}} \right)^2 \sqrt{\frac{GM_t}{r_{in}^3}}. \quad (17)$$

Fig. 8 plots the  $\nu_d$  value given by equation (17) as a function of  $p$ . Depending on the disc outer radius, we clearly see a measurement of  $\nu_d$  can constrain the  $p$  value of the disc. The model parameters from Table 4 support  $p \sim 1$ , which differs substantially from the Fang et al. (2019) constraint of  $p \approx -2.9$ . However, we note that this discrepancy relies on the disc [O I] emission arising from a gaseous disc associated with the occulting ring, as opposed to the interpretation given by Mundt et al. (2010), who argued the [O I] emission originated from a bipolar jet associated with one or both of the stars at the centre of KH 15D. Further photometric modelling is required to see if the  $p$  value implied by the disc precession frequency differs from that constrained by the disc O I emission.

#### 4 THEORETICAL IMPLICATIONS OF DYNAMICAL WARPED DISC MODEL

In Section 3, we showed how the photometry of KH 15D could be explained by a precessing circumbinary disc, in agreement with the results of other works (Chiang & Murray-Clay 2004; Winn et al. 2004, 2006; Silvia & Agol 2008). The parameters constrained by

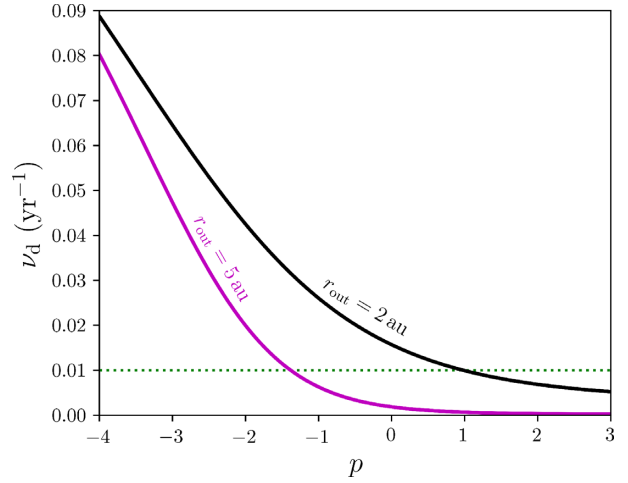


**Figure 8.** Global disc precession frequency  $\nu_d$  (equation 17) as a function of the surface density power-law index  $p$  ( $\Sigma \propto r^p$ ), for the KH 15D system parameters, assuming  $r_{in} = 0.5$  au with the  $r_{out}$  values indicated. Dotted green line shows our dynamical model value of  $\nu_d = 0.01 \text{ yr}^{-1}$ . Depending on the disc radial extent, a measurement of  $\nu_d$  translates to a constraint on  $p$ .

the photometry of the system are listed in Table 4. Although the fit of the dynamical model to the photometry is crude, we argue the basic conclusions on the parameters of the system are unlikely to differ by more than a factor of a few, and comprises some of the first constraints on small warps within protoplanetary discs. This section connects the constraints of our dynamical model to theories describing warp propagation in accretion discs, as well as speculation on the long-term evolution of the system. We also discuss predictions from our model, as well as future modelling efforts.

#### 4.1 Explaining the warp and twist within KH 15D

Our dynamical model requires a non-zero warp ( $\Delta I = I_T - I_L$ ) and twist ( $\Delta \Omega = \Omega_T - \Omega_L$ ) to cause the complex series of occultations seen in the KH 15D system. These warps and twists arise from the disc resisting the differential nodal precession induced by the specific torque of the binary

$$|T_{bin}| \sim r^2 n \nu |\bar{I}|, \quad (18)$$

where  $n = \sqrt{GM_t/r^3}$  is the rings orbital frequency,  $\nu$  is the characteristic nodal precession frequency induced on the disc from the binary (equation 6), and  $\bar{I}$  is the characteristic ‘average’ inclination of the disc. One way to balance the torque from the binary is by thermal pressure between ringlets, which has an internal torque of order (e.g. Ogilvie 1999; Chiang & Culter 2003; Chiang & Murray-Clay 2004)

$$|T_{press}| \sim c_s^2 |\Delta I|, \quad (19)$$

where  $c_s = h n$  is the ring sound speed, while  $h$  is the aspect ratio of the disc. Assuming torque balance ( $|T_{press}| \approx |T_{bin}|$ ) allows us to estimate the warp which may develop under the resisting influence of thermal pressure:

$$\left| \frac{\Delta I}{\bar{I}} \right|_{press} \sim \frac{r^2 n \nu}{c_s^2} \bigg|_{r=\bar{r}} = 13 \left( \frac{0.05}{h} \right)^2 \left( \frac{\mu}{0.33 M_\odot} \right) \left( \frac{1.32 M_\odot}{M_t} \right) \times \left( \frac{a}{0.29 \text{ au}} \right)^2 \left( \frac{0.7 \text{ au}}{\bar{r}} \right)^2, \quad (20)$$

where  $\bar{r}$  is some characteristic radius within the disc. Clearly, this warp is quite large.

However, in nearly inviscid (Shakura–Sunyaev parameter  $\alpha \lesssim h$ ) discs with the radial-epicyclic frequency satisfying  $\kappa^2 \approx n^2$ , the near-resonant propagation of bending waves across the disc can amplify the strength of the hydrodynamical torque by a factor (Papaloizou & Lin 1995; Lubow & Ogilvie 2000; Ogilvie 2006)

$$|T_{\text{bw}}| \sim \frac{1}{|\tilde{\kappa}|} |T_{\text{press}}|, \quad (21)$$

where  $\tilde{\kappa} \equiv (\kappa^2 - n^2)/(2n^2)$  is a dimensionless quantity related to the apsidal precession rate. Because the secular apsidal precession rate is  $|\tilde{\kappa}| \sim \nu/n$  for circumbinary discs (Miranda & Lai 2015), torque balance ( $|T_{\text{bw}}| \approx |T_{\text{bin}}|$ ) gives

$$\left| \frac{\Delta I}{\bar{I}} \right|_{\text{bw}} \sim \frac{r^2 \nu^2}{c_s^2} \bigg|_{r=\bar{r}} = 0.42 \left( \frac{0.05}{h} \right)^2 \left( \frac{\mu}{0.33 M_\odot} \right)^2 \left( \frac{1.32 M_\odot}{M_t} \right)^2 \times \left( \frac{a}{0.29 \text{ au}} \right)^4 \left( \frac{0.7 \text{ au}}{\bar{r}} \right)^4. \quad (22)$$

This estimate is much closer to the  $|\Delta I/\bar{I}| \sim 1$  values implied by our dynamical model, and lies in agreement with more detailed calculations of warp propagation in protoplanetary discs (Foucart & Lai 2013, 2014; Lodato & Facchini 2013; Lubow & Martin 2018; Zanazzi & Lai 2018).

Disc self-gravity can also resist differential nodal precession from the binary. Mutually misaligned ringlets experience specific mutual internal torques of order (Chiang & Culter 2003; Chiang & Murray-Clay 2004; Tremaine & Davis 2014; Zanazzi & Lai 2017; Batygin 2018)

$$|T_{\text{sg}}| \sim \frac{G \Sigma r}{h} |\Delta I| \sim \frac{G M_d}{h r} |\Delta I|, \quad (23)$$

assuming the disc mass  $M_d \sim r^2 \Sigma$ , and the additional factor of  $h^{-1}$  arises from the enhancement of the mutual gravitational attraction between ringlets when the disc is vertically thin (Batygin 2018). Torque balance ( $|T_{\text{sg}}| \approx |T_{\text{bin}}|$ ) leads to warps of order

$$\left| \frac{\Delta I}{\bar{I}} \right|_{\text{sg}} \sim \frac{r^3 n \nu h}{G M_d} \bigg|_{r=\bar{r}} = 1.3 \left( \frac{h}{0.05} \right) \left( \frac{\mu}{0.33 M_\odot} \right) \left( \frac{1.7 M_{\text{Jup}}}{M_d} \right) \times \left( \frac{a}{0.29 \text{ au}} \right)^2 \left( \frac{0.7 \text{ au}}{\bar{r}} \right)^2. \quad (24)$$

Even after assuming the upper limit on the total (gas and dust) disc mass inferred by ALMA observations (Aronow et al. 2018), self-gravity is typically not as effective as bending waves at enforcing coplanarity between ringlets. However, a massive disc ( $M_d \sim 1 M_{\text{Jup}}$ ) can give warps comparable to those inferred by our dynamical KH 15D disc model.

The direction of the warp ( $\Delta I$  positive or negative) has also been argued to encode information on the internal forces/torques enforcing disc coplanarity. Chiang & Murray-Clay (2004) argued thermal pressure predicts  $\Delta I < 0$ , while self-gravity predicts  $\Delta I > 0$ . More detailed calculations support the prediction that a disc should relax to a  $\Delta I > 0$  profile under the influence of disc self-gravity (Batygin 2012, 2018; Zanazzi & Lai 2017). But calculations taking into account the resonant propagation of bending waves *also* predict  $\Delta I > 0$  (e.g. Facchini et al. 2013; Foucart & Lai 2014; Lubow & Martin 2018; Zanazzi & Lai 2018). Hydrodynamical simulations of protoplanetary discs (neglecting self-gravity) find conflicting results, with  $\Delta I > 0$  and  $\Delta I < 0$  at different times, primarily because the simulations usually cannot be run long enough for the system to relax to a smoothly evolving warp profile (e.g. Facchini et al. 2013; Martin & Lubow 2017, 2018; Moody, Shi & Stone 2019; Smallwood et al.

2019, 2020). We note that the disc may never relax to a steady state. Simulations which accurately calculate how the binary interacts with a tidally truncated circumbinary disc find highly dynamical inner disc edges for discs orbiting eccentric binaries (e.g. Miranda, Muñoz & Lai 2017; Franchini, Lubow & Martin 2019; Muñoz, Miranda & Lai 2019; Muñoz et al. 2020). Because resonant Lindblad torques often truncate discs (e.g. Artymowicz & Lubow 1994; Lubow, Martin & Nixon 2015; Miranda & Lai 2015), which may also excite disc tilts (Borderies, Goldreich & Tremaine 1984; Lubow 1992; Zhang & Lai 2006), it is not unreasonable to say a real circumbinary disc may never relax to a steady-state inclination profile. We conclude that bending-wave propagation is the main internal force enforcing rigid precession of the disc of KH 15D, despite the conflicting predictions for the sign of  $\Delta I$ .

A small viscosity in a circumbinary disc also leads to a non-zero twist, due to the azimuthal shear induced by differential nodal precession. The magnitude of the torque resisting nodal shear is (Papaloizou & Pringle 1983; Papaloizou & Lin 1995; Ogilvie 1999; Lubow & Ogilvie 2000)

$$|T_{\text{visc}}| \sim \frac{1}{\alpha} c_s^2 |\Delta \Omega|, \quad (25)$$

assuming an isotropic kinematic viscosity ( $\nu = \alpha p / [\rho n]$ ). The  $\alpha^{-1}$  (rather than  $\alpha^{+1}$ ) dependence in equation (25) is from near-resonant forcing of radial and azimuthal perturbations (since  $\kappa^2 \approx n^2$ ), which are damped only by viscosity (Papaloizou & Lin 1995; Lubow & Ogilvie 2000; Lodato & Pringle 2007). Viscosity leads to twists of order (assuming  $|T_{\text{visc}}| \approx |T_{\text{bin}}|$ )

$$\left| \frac{\Delta \Omega}{\bar{I}} \right|_{\text{visc}} \sim \frac{\alpha r^2 n \nu}{c_s^2} \bigg|_{r=\bar{r}} = 0.13 \left( \frac{\alpha}{0.01} \right) \left( \frac{0.05}{h} \right)^2 \times \left( \frac{\mu}{0.33 M_\odot} \right) \left( \frac{1.32 M_\odot}{M_t} \right) \times \left( \frac{a}{0.29 \text{ au}} \right)^2 \left( \frac{0.7 \text{ au}}{\bar{r}} \right)^2. \quad (26)$$

More detailed calculations typically give positive  $\Delta \Omega$  values a bit larger in circumbinary discs (Foucart & Lai 2014; Zanazzi & Lai 2018), in agreement with our dynamical model. Although observations frequently infer  $\alpha$  values much lower than  $10^{-2}$  (e.g. Hughes et al. 2011; Flaherty et al. 2015; Teague et al. 2016; Rafikov 2017; Ansdell et al. 2018), the large warp in this disc can excite parametric instabilities, enhancing the viscous dissipation rate in the disc (Goodman 1993; Ryu & Goodman 1994; Gammie, Goodman & Ogilvie 2000; Ogilvie & Latter 2013; Paardekooper & Ogilvie 2019).

The arguments above slightly favour a disc held together by resonant bending waves over self-gravity. However, such an interpretation requires the scale height of the gas be much higher than that of the solids (dust, pebbles, or planetesimals), which must be sufficiently small to cause the sharp occultations seen in the KH 15D light curve ( $H_{\text{solid}} \lesssim R_A, R_B$ ). Although no firm detection of disc gas within the KH 15D system has been made, Lawler et al. (2010) detected Na I D line emission and absorption from KH 15D, with a column density that did not vary as the stars became more inclined to the disc mid-plane. If the Na I D emission/absorption is from the disc gas (not the interstellar medium), this implies a large gas scale height ( $H_{\text{gas}} \gg R_A, R_B$ ). A discrepancy between the gas and solid scale heights is expected theoretically, as aerodynamical drag causes particles to settle to the disc mid-plane (e.g. Youdin & Lithwick 2007). Without gas, dust/solids/planetesimals tend to have larger scale heights due to

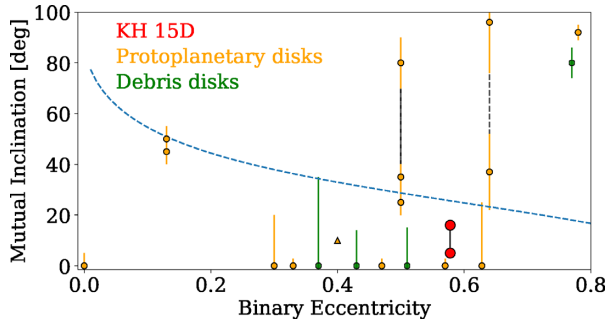


**Figure 9.** The mutual inclination between the disc and binary orbital plane in the KH 15D system (red), plotted alongside circumbinary disc inclinations for protoplanetary (orange) and debris (green) discs (Czekala et al. 2019), as a function of binary eccentricity. The dashed blue lines plot the critical inclination (equation 27). The black dotted lines connect degenerate solutions for HD 142527, SR 24N, and GG Tau Aa-Ab. The triangle represents the lower limit for R CrA. The disc in KH 15D will align (not polar align) with the orbital plane of the binary.

mutual gravitational interactions that excite particle inclinations (e.g. Goldreich, Lithwick & Sari 2004). Moreover, if the disc has no gas, because the solids must be optically thick to starlight, the required solid densities would cause frequent collisions between particles, and imply the KH 15D disc has a short lifetime (e.g. Wyatt 2008).

We conclude the disc warp and twist implied by our model lie in accord with hydrodynamical theories of warped accretion discs.

#### 4.2 Long-term dynamical evolution of KH 15D

Recently, Czekala et al. (2019) showed circumbinary discs (both gas and debris) have higher inclinations when orbiting eccentric binaries. Fig. 9 displays the disc inclinations analysed in Czekala et al. (2019), alongside our constraints for the inclination of KH 15D, which we take directly from our photometric fits ( $|\theta_T[t_3]| \lesssim |I_{\text{KH 15D}}| \lesssim |\theta_L[t_3]|$ , see Section 3.2). The dashed blue line displays the critical inclination (Aly et al. 2015; Martin & Lubow 2017; Zanazzi & Lai 2018)

$$I_{\text{crit}} = \cos^{-1} \sqrt{\frac{5e^2}{1+4e^2}}, \quad (27)$$

which is a necessary (but not sufficient) condition for the disc–binary inclination to evolve to  $90^\circ$  (polar alignment). From Fig. 9, because  $|I_{\text{crit}}| > |I_{\text{KH 15D}}|$ , we can be confident the disc will not polar align, and will eventually align with the orbital plane of the binary (without any other mechanisms exciting the disc inclination).

We can also estimate the time-scale over which the disc inclination evolves. Because a non-zero twist  $\Delta\Omega$  exerts a backreaction torque on the disc from the binary, the disc is driven into alignment (or polar alignment) over the time-scale (Foucart & Lai 2014; Zanazzi & Lai 2018)

$$\gamma_{\text{evol}} \sim \nu_d |\Delta\Omega|. \quad (28)$$

Inserting equation (26) into equation (28) gives the often-quoted ‘Bate time-scale’ (Bate et al. 2000). However, because  $\nu_d$  and  $\Delta\Omega$  are both determined by our dynamical model, we can actually estimate  $\gamma_{\text{evol}}$  using *observationally inferred parameters*:

$$\gamma_{\text{evol}} \sim 2.6 \times 10^{-3} \left( \frac{\nu_d}{0.01 \text{ yr}^{-1}} \right) \left( \frac{\Delta\Omega}{15^\circ} \right) \text{ yr}^{-1}. \quad (29)$$

Equation (29) implies the disc should align with the orbital plane of the binary in less than  $\sim 10^3$  yr. Although secular interactions can

**Table 3.** An excerpt from Table 3. For interested observers, the full version (available in machine-readable form) includes *I*-band magnitude predictions for the years 2000–2050 from our light-curve model of KH 15D as shown in Figs 3–5.

Julian date	Gregorian date	KH 15D <i>I</i> -band magnitude
2451545.0	2000.000	14.509
2451546.0	2000.003	14.507
2451547.0	2000.005	14.506
...	...	...
2469807.0	2049.999	13.462

**Table 4.** Parameter values for our dynamical model of a warped disc precessing around an eccentric binary in the KH 15D system. Disc inclinations are relative to the binary orbital plane, and disc longitude of ascending nodes are relative to the binary pericentre direction. See text for definitions and discussion.

Parameter	Example value
$\nu_d$ ( $\text{yr}^{-1}$ )	0.01
$r_L$ (au)	0.5
$r_T$ (au)	2.0
$I_L(t_3)$ (deg)	−13
$I_T(t_3)$ (deg)	−6
$\Omega_L(t_3)$ (deg)	100
$\Omega_T(t_3)$ (deg)	115

keep the disc misaligned with the eccentric orbital plane of the binary over time-scales a few times longer than estimate (29) (Zanazzi & Lai 2018; Smallwood et al. 2019), this is much shorter than the  $\sim 10^6$  yr lifetimes of typical protoplanetary discs (e.g. Haisch, Lada & Lada 2001). Either we are observing KH 15D while it is still very young, or additional mechanisms are exciting the disc inclination.

#### 4.3 KH 15D model predictions and improvements

The most immediate consequences are predictions for future light curve behaviour from our photometry model fits (Figs 3 and 5, Table 2). Current *I*-band measurements should show the light from star A slowly being revealed by the trailing edge (since  $t_7 \approx 2021$ ). By the year  $\sim 2029$ , the orbit of star B should be completely revealed, resulting in a ceasing of the variability from this star. By the year  $\sim 2041$ , we should cease to see photometric variability due to the circumbinary disc. While our current model which produces a reasonable fit to the photometric data employs an opaque screen with a constant  $\dot{\theta}_T$ , our dynamical model predicts that the fit can be further improved if the change of  $\dot{\theta}_T$  with time is incorporated (equation 11). We provide in Table 3 the predicted light curve (in *I* band) of this system until the year 2050.

We are able to make an explicit connection between the phenomenological model (Section 2), and a precessing, warped disc occulting the binary of KH 15D (Section 3). More stringent constraints on the disc geometry would use the inner and outer disc orbital parameters  $\{r_k, I_k, \Omega_k\}$  and global disc precession frequency  $\nu_d$ , rather than parameters describing the locations and orientations of the leading and trailing edges  $\{\theta_k, \dot{\theta}_k, Y_k, \dot{Y}_k\}$ , to fit the light curve of KH 15D. This exercise should yield parameters consistent with those listed in Table 4 within a factor of a few.

Our folded light curves (Figs 4 and 5) show the leading edge is well fitted by a sharp edge, whereas the poor fit for the trailing edge imply it is clumpy/puffy, in agreement with the findings of García Soto



et al. (2020). The sharp inner edge is likely due to tidal truncation by the torque from the binary. Calculations and hydrodynamical simulations suggest that the radius at which the binary truncates the disc is  $\sim 2$  times the binary semimajor axis ( $a \approx 0.3$  au) (e.g. Miranda & Lai 2015), lying close to the inner radius value of our dynamical model (Table 4). However, it remains unclear why the disc is so compact ( $r_{\text{out}} \lesssim 5$  au), and the possibility still exists the disc outer edge is truncated by a planet (Chiang & Murray-Clay 2004). There exists tentative observational support for this hypothesis, as Arulanantham et al. (2017) found infrared-excess from KH 15D consistent with the thermal emission from a  $\sim 10 M_{\text{Jup}}$  mass planet. Future modelling of how dust scattering and the finite optical depth of the disc can create a ‘fuzzier’ outer edge would be of interest (Chiang & Murray-Clay 2004; Silvia & Agol 2008).

## 5 CONCLUSIONS

In this work, we have developed a circumbinary disc model that explains the photometric variability of KH 15D spanning more than 60 yr. From this model, we are able to constrain the disc annular extent, inclination, orientation with respect to the binary pericentre direction, warp profile, precession frequency, and even surface density profile. The fits of our phenomenological model to fit the photometry of KH 15D are displayed in Table 2, with parameters of a warped disc which are consistent with the phenomenological model constraints listed in Table 4. Although strict constraints on the warped disc remain elusive, we can be confident about the following features of the disc:

- (i) The beginning of the dips/occultations in KH 15D is due to the disc inner edge slowly covering the binary, while the currently observed slow reversal of the dipping behaviour in KH 15D is due to the disc outer edge slowly revealing the binary. The inner edge has a radius  $r_{\text{in}} \lesssim 1$  au, while the outer edge has a radius  $r_{\text{out}} \sim \text{few au}$ .
- (ii) The disc inner edge is more inclined to the orbital plane of the binary than the disc outer edge. Both inner and outer disc inclinations are less than  $\sim 16^\circ$ , but greater than  $\sim 5^\circ$ , with a difference of order  $\sim 10^\circ$ .
- (iii) The disc inner and outer longitude of ascending nodes differ by  $\sim 15^\circ$ .

These constraints are consistent with hydrodynamical theories of warped accretion discs, resisting differential nodal precession from the gravitational torque from the binary (Section 4.1).

Our models also find a precessional period of order  $P_{\text{prec}} \sim 2\pi/\nu_d \sim 600$  yr, but this constraint is sensitive to the model fit of KH 15D. We can be very confident, however, that the time-scale over which the disc of KH 15D aligns with the orbital plane of the binary is much shorter than the lifetime of the disc (equation 29), suggesting that additional mechanisms are exciting the disc tilt.

## ACKNOWLEDGEMENTS

We thank Eugene Chiang, Ruth Murray-Clay, and Norm Murray for useful discussions, and Jessica Speedie for help in developing the circumbinary disc visualization in Fig. 1. We would also like to thank the referee, William Herbst, for comments and suggestions that have improved the quality of this work. MP has been supported by undergraduate research fellowships from the Centre for Planetary Sciences and Canadian Institute for Theoretical Astrophysics (CITA). JZ and WZ were supported by the Natural Sciences and Engineering Research Council of Canada (NSERC) under the funding reference # CITA 490888-16.

## DATA AVAILABILITY

The data underlying this article are available in the public domain (Hamilton et al. 2003; Johnson & Winn 2004; Johnson et al. 2004; Maffei, Ciprini & Tosti 2005; Winn et al. 2006; Aronow et al. 2018; García Soto et al. 2020). The data produced in this work are available in its online supplementary material (Table 3).

## REFERENCES

- Aly H., Lodato G., 2020, *MNRAS*, 492, 3306
- Aly H., Dehnen W., Nixon C., King A., 2015, *MNRAS*, 449, 65
- Andrews S. M., Czekala I., Wilner D. J., Espaillat C., Dullemond C. P., Hughes A. M., 2010, *ApJ*, 710, 462
- Andrews S. M. et al., 2012, *ApJ*, 744, 162
- Ansdeell M. et al., 2018, *ApJ*, 859, 21
- Armstrong D. J., Osborn H. P., Brown D. J. A., Faedi F., Gómez Maqueo Chew Y., Martin D. V., Pollacco D., Udry S., 2014, *MNRAS*, 444, 1873
- Aronow R. A., Herbst W., Hughes A. M., Wilner D. J., Winn J. N., 2018, *AJ*, 155, 47
- Artymowicz P., Lubow S. H., 1994, *ApJ*, 421, 651
- Arulanantham N. A., Herbst W., Gilmore M. S., Cauley P. W., Leggett S. K., 2017, *ApJ*, 834, 119
- Bate M. R., Bonnell I. A., Clarke C. J., Lubow S. H., Ogilvie G. I., Pringle J. E., Tout C. A., 2000, *MNRAS*, 317, 773
- Bate M. R., Bonnell I. A., Bromm V., 2002, *MNRAS*, 336, 705
- Bate M. R., 2012, *MNRAS*, 419, 3115
- Bate M. R., 2018, *MNRAS*, 475, 5618
- Batygin K., 2012, *Nature*, 491, 418
- Batygin K., 2018, *MNRAS*, 475, 5070
- Bi J. et al., 2020, *ApJ*, 895, L18
- Birnstiel T., Andrews S. M., 2014, *ApJ*, 780, 153
- Borderies N., Goldreich P., Tremaine S., 1984, *ApJ*, 284, 429
- Brinch C., Jørgensen J. K., Hogerheijde M. R., Nelson R. P., Gressel O., 2016, *ApJ*, 830, L16
- Capelo H. L., Herbst W., Leggett S. K., Hamilton C. M., Johnson J. A., 2012, *ApJ*, 757, L18
- Chen C., Franchini A., Lubow S. H., Martin R. G., 2019, *MNRAS*, 490, 5634
- Chen C., Lubow S. H., Martin R. G., 2020, *MNRAS*, 494, 4645
- Chiang E. I., Culter C. J., 2003, *ApJ*, 599, 675
- Chiang E. I., Murray-Clay R. A., 2004, *ApJ*, 607, 913
- Czekala I., Andrews S. M., Jensen E. L. N., Stassun K. G., Torres G., Wilner D. J., 2015, *ApJ*, 806, 154
- Czekala I., Andrews S. M., Torres G., Jensen E. L. N., Stassun K. G., Wilner D. J., Latham D. W., 2016, *ApJ*, 818, 156
- Czekala I. et al., 2017, *ApJ*, 851, 132
- Czekala I., Chiang E., Andrews S. M., Jensen E. L. N., Torres G., Wilner D. J., Stassun K. G., Macintosh B., 2019, *ApJ*, 883, 22
- de Gregorio-Monsalvo I. et al., 2013, *A&A*, 557, A133
- Doolin S., Blundell K. M., 2011, *MNRAS*, 418, 2656
- Doyle L. R., Deeg H. J., 2018, *The Way to Circumbinary Planets*. Springer, Cham, Switzerland, p. 115
- Facchini S., Lodato G., Price D. J., 2013, *MNRAS*, 433, 2142
- Facchini S., Juhász A., Lodato G., 2018, *MNRAS*, 473, 4459
- Facchini S. et al., 2019, *A&A*, 626, L2
- Fang M., Pascucci I., Kim J. S., Edwards S., 2019, *ApJ*, 879, L10
- Farago F., Laskar J., 2010, *MNRAS*, 401, 1189
- Flaherty K. M., Hughes A. M., Rosenfeld K. A., Andrews S. M., Chiang E., Simon J. B., Kerzner S., Wilner D. J., 2015, *ApJ*, 813, 99
- Foreman-Mackey D., Hogg D. W., Lang D., Goodman J., 2013, *PASP*, 125, 306
- Foucart F., Lai D., 2013, *ApJ*, 764, 106
- Foucart F., Lai D., 2014, *MNRAS*, 445, 1731
- Franchini A., Lubow S. H., Martin R. G., 2019, *ApJ*, 880, L18
- Francis L., van der Marel N., 2020, *ApJ*, 892, 111
- Fulton B. J., Petigura E. A., Blunt S., Sinukoff E., 2018, *PASP*, 130, 044504
- Gammie C. F., Goodman J., Ogilvie G. I., 2000, *MNRAS*, 318, 1005

- García Soto A., Ali A., Newmark A., Herbst W., Windemuth D., Winn J. N., 2020, *AJ*, 159, 135
- Giuppone C. A., Cuello N., 2019, *J. Phys. Conf. Ser.*, 1365, 012023
- Goldreich P., Lithwick Y., Sari R., 2004, *ARA&A*, 42, 549
- Goodman J., 1993, *ApJ*, 406, 596
- Haisch, Karl E. J., Lada E. A., Lada C. J., 2001, *ApJ*, 553, L153
- Hamilton C. M., Herbst W., Mundt R., Bailer-Jones C. A. L., Johns-Krull C. M., 2003, *ApJ*, 591, L45
- Hamilton C. M. et al., 2005, *AJ*, 130, 1896
- Hughes A. M., Wilner D. J., Andrews S. M., Qi C., Hogerheijde M. R., 2011, *ApJ*, 727, 85
- Johnson J. A., Winn J. N., 2004, *AJ*, 127, 2344
- Johnson J. A., Marcy G. W., Hamilton C. M., Herbst W., Johns-Krull C. M., 2004, *AJ*, 128, 1265
- Kearns K. E., Herbst W., 1998, *ApJ*, 116, 261
- Kennedy G. M. et al., 2012a, *MNRAS*, 421, 2264
- Kennedy G. M., Wyatt M. C., Sibthorpe B., Phillips N. M., Matthews B. C., Greaves J. S., 2012b, *MNRAS*, 426, 2115
- Kennedy G. M. et al., 2019, *Nat. Astron.*, 3, 230
- Kraus S. et al., 2020, *Science*, 369, 1233
- Larwood J. D., Papaloizou J. C. B., 1997, *MNRAS*, 285, 288
- Lawler S. M., Herbst W., Redfield S., Hamilton C. M., Johns-Krull C. M., Winn J. N., Johnson J. A., Mundt R., 2010, *ApJ*, 711, 1297
- Li G., Holman M. J., Tao M., 2016, *ApJ*, 831, 96
- Lodato G., Facchini S., 2013, *MNRAS*, 433, 2157
- Lodato G., Pringle J. E., 2007, *MNRAS*, 381, 1287
- Lubow S. H., 1992, *ApJ*, 398, 525
- Lubow S. H., Martin R. G., 2018, *MNRAS*, 473, 3733
- Lubow S. H., Ogilvie G. I., 2000, *ApJ*, 538, 326
- Lubow S. H., Martin R. G., Nixon C., 2015, *ApJ*, 800, 96
- McLaughlin D. B., 1924, *ApJ*, 60, 22
- Maffei P., Ciprini S., Tosti G., 2005, *MNRAS*, 357, 1059
- Marino S., Perez S., Casassus S., 2015, *ApJ*, 798, L44
- Martin R. G., Lubow S. H., 2017, *ApJ*, 835, L28
- Martin R. G., Lubow S. H., 2018, *MNRAS*, 479, 1297
- Martin D. V., Triaud A. H. M. J., 2014, *A&A*, 570, A91
- Miranda R., Lai D., 2015, *MNRAS*, 452, 2396
- Miranda R., Muñoz D. J., Lai D., 2017, *MNRAS*, 466, 1170
- Moody M. S. L., Shi J.-M., Stone J. M., 2019, *ApJ*, 875, 66
- Mundt R., Hamilton C. M., Herbst W., Johns-Krull C. M., Winn J. N., 2010, *ApJ*, 708, L5
- Muñoz D. J., Miranda R., Lai D., 2019, *ApJ*, 871, 84
- Muñoz D. J., Lai D., Kratter K., Miranda R., 2020, *ApJ*, 889, 114
- Nixon C., King A., Price D., 2013, *MNRAS*, 434, 1946
- Ogilvie G. I., 1999, *MNRAS*, 304, 557
- Ogilvie G. I., 2006, *MNRAS*, 365, 977
- Ogilvie G. I., Latter H. N., 2013, *MNRAS*, 433, 2420
- Paardekooper S.-J., Ogilvie G. I., 2019, *MNRAS*, 483, 3738
- Panić O., Hogerheijde M. R., Wilner D., Qi C., 2009, *A&A*, 501, 269
- Papaloizou J. C. B., Lin D. N. C., 1995, *ApJ*, 438, 841
- Papaloizou J. C. B., Pringle J. E., 1983, *MNRAS*, 202, 1181
- Pegues J. et al., 2021, *ApJ*, 908, 42
- Poblete P. P., Cuello N., Cuadra J., 2019, *MNRAS*, 489, 2204
- Poblete P. P., Calcino J., Cuello N., Macías E., Ribas Á., Price D. J., Cuadra J., Pinte C., 2020, *MNRAS*, 496, 2362
- Powell D., Murray-Clay R., Schlichting H. E., 2017, *ApJ*, 840, 93
- Price D. J. et al., 2018, *MNRAS*, 477, 1270
- Rafikov R. R., 2017, *ApJ*, 837, 163
- Rosenfeld K. A., Andrews S. M., Wilner D. J., Stempels H. C., 2012, *ApJ*, 759, 119
- Rosotti G. P., Tazzari M., Booth R. A., Testi L., Lodato G., Clarke C., 2019, *MNRAS*, 486, 4829
- Rossiter R. A., 1924, *ApJ*, 60, 15
- Ruíz-Rodríguez D., Kastner J. H., Dong R., Principe D. A., Andrews S. M., Wilner D. J., 2019, *AJ*, 157, 237
- Ryu D., Goodman J., 1994, *ApJ*, 422, 269
- Silvia D. W., Agol E., 2008, *ApJ*, 681, 1377
- Smallwood J. L., Lubow S. H., Franchini A., Martin R. G., 2019, *MNRAS*, 486, 2919
- Smallwood J. L., Franchini A., Chen C., Becerril E., Lubow S. H., Yang C.-C., Martin R. G., 2020, *MNRAS*, 494, 487
- Takeuchi T., Lin D. N. C., 2002, *ApJ*, 581, 1344
- Teague R. et al., 2016, *A&A*, 592, A49
- Tremaine S., Davis S. W., 2014, *MNRAS*, 441, 1408
- Weidenschilling S. J., 1977, *MNRAS*, 180, 57
- Welsh W. F., Orosz J. A., 2018, *Two Suns in the Sky: The Kepler Circumbinary Planets*. Springer, Cham, Switzerland, p. 34
- Winn J. N., Holman M. J., Johnson J. A., Stanek K. Z., Garnavich P. M., 2004, *ApJ*, 603, L45
- Winn J. N., Hamilton C. M., Herbst W. J., Hoffman J. L., Holman M. J., Johnson J. A., Kuchner M. J., 2006, *ApJ*, 644, 510
- Wyatt M. C., 2008, *ARA&A*, 46, 339
- Youdin A. N., Lithwick Y., 2007, *Icarus*, 192, 588
- Zanazzi J. J., Lai D., 2017, *MNRAS*, 464, 3945
- Zanazzi J. J., Lai D., 2018, *MNRAS*, 473, 603
- Zhang Z., Fabrycky D. C., 2019, *ApJ*, 879, 92
- Zhang H., Lai D., 2006, *MNRAS*, 368, 917

## SUPPORTING INFORMATION

Supplementary data are available at *MNRAS* online.

**Table 3.** An excerpt from Table 3. For interested observers.

Please note: Oxford University Press is not responsible for the content or functionality of any supporting materials supplied by the authors. Any queries (other than missing material) should be directed to the corresponding author for the article.

## APPENDIX A: MODEL PARAMETERS

We display all MCMC parameter fits for our new photometric model, for various  $\alpha$ , as described in Section 2.2. Recall  $\alpha$  is the ratio of the trail edge velocity over the lead edge velocity along the vertical axis of our line of sight. Small  $\alpha$  tests for narrow disc models whereas large  $\alpha$  tests for extended disc models. We do not report model parameters for  $\alpha = 10.0$  since the MCMC does not converge. Upper and lower error bars indicate a  $1\sigma$  confidence interval. Model parameters are described in Table 1.

**Table A1.** Same as Table 2, except we vary the value of  $\alpha$ .

Free parameter	$\alpha = 0.1$	$\alpha = 0.3$	$\alpha = 2.0$	$\alpha = 3.0$
$P$ (d)	$48.3786^{+0.0002}_{-0.0002}$	$48.3781^{+0.0002}_{-0.0002}$	$48.3713^{+0.0002}_{-0.0002}$	$48.3691^{+0.0002}_{-0.0001}$
$e$	$0.5794^{+0.0008}_{-0.0008}$	$0.5771^{+0.0009}_{-0.0009}$	$0.5716^{+0.0008}_{-0.0008}$	$0.5677^{+0.0008}_{-0.0008}$
$I$ (deg)	$91.002^{+0.003}_{-0.001}$	$91.002^{+0.003}_{-0.001}$	$91.0004^{+0.0008}_{-0.0003}$	$91.0005^{+0.0008}_{-0.0003}$
$\omega$ (deg)	$9.80^{+0.05}_{-0.06}$	$11.29^{+0.06}_{-0.06}$	$12.04^{+0.06}_{-0.06}$	$11.97^{+0.06}_{-0.07}$
$T_p$ (JD) – 2452 350	$3.48^{+0.02}_{-0.01}$	$4.00^{+0.02}_{-0.02}$	$4.32^{+0.02}_{-0.02}$	$4.31^{+0.02}_{-0.02}$
$L_B/L_A$	$1.63^{+0.01}_{-0.02}$	$1.57^{+0.02}_{-0.01}$	$1.17^{+0.01}_{-0.01}$	$1.064^{+0.009}_{-0.009}$
$\epsilon_1$	$0.0516^{+0.0008}_{-0.0008}$	$0.0481^{+0.0007}_{-0.0007}$	$0.071^{+0.001}_{-0.001}$	$0.085^{+0.001}_{-0.001}$
$\epsilon_2$	$0.097^{+0.001}_{-0.001}$	$0.0651^{+0.0009}_{-0.0009}$	$0.0495^{+0.0006}_{-0.0007}$	$0.0499^{+0.0007}_{-0.0007}$
$\xi_1$	$1.81^{+0.03}_{-0.04}$	$1.44^{+0.02}_{-0.02}$	$2.40^{+0.04}_{-0.04}$	$3.18^{+0.07}_{-0.06}$
$\xi_2$	$7.5^{+0.2}_{-0.2}$	$3.60^{+0.07}_{-0.06}$	$2.97^{+0.05}_{-0.05}$	$3.04^{+0.05}_{-0.05}$
$t_3$	$1992.70^{+0.06}_{-0.06}$	$1993.16^{+0.05}_{-0.05}$	$1991.49^{+0.07}_{-0.08}$	$1991.3^{+0.1}_{-0.1}$
$t_5$	$2008.16^{+0.01}_{-0.01}$	$2008.12^{+0.01}_{-0.01}$	$2007.72^{+0.01}_{-0.01}$	$2007.76^{+0.02}_{-0.02}$
$t_6$	$2013.18^{+0.03}_{-0.03}$	$2013.46^{+0.03}_{-0.03}$	$2012.44^{+0.02}_{-0.02}$	$2012.07^{+0.02}_{-0.02}$
$\theta_L(t_3)$ (deg)	$-55^{+1}_{-1}$	$-20.0^{+0.3}_{-0.3}$	$-13.5^{+0.2}_{-0.2}$	$-13.7^{+0.2}_{-0.2}$
$\theta_T(t_3)$ (deg)	$-2.7^{+0.4}_{-0.4}$	$-2.4^{+0.2}_{-0.2}$	$-21.0^{+0.3}_{-0.3}$	$-29.7^{+0.4}_{-0.5}$
$\dot{\theta}_{L1}$ (rad yr $^{-1}$ )	$0.0075^{+0.0004}_{-0.0005}$	$0.0099^{+0.0002}_{-0.0003}$	$0.0025^{+0.0002}_{-0.0002}$	$0.0019^{+0.0003}_{-0.0003}$
$\dot{\theta}_{L2}$ (rad yr $^{-1}$ )	$0.0093^{+0.0003}_{-0.0003}$	$0.0033^{+0.0002}_{-0.0002}$	$0.0042^{+0.0001}_{-0.0001}$	$0.0046^{+0.0001}_{-0.0001}$
$\dot{\theta}_T$ (rad yr $^{-1}$ )	$-0.0035^{+0.0003}_{-0.0003}$	$-0.0030^{+0.0001}_{-0.0001}$	$0.0065^{+0.0002}_{-0.0002}$	$0.0088^{+0.0003}_{-0.0003}$
Fit photometry?	No	Yes	No	No
$\chi^2_{\text{phot}}$	16 386	13 822	15 558	17 222
$\chi^2_{\text{RV}}$	12	13	16	17
Reduced $\chi^2$	1.62	1.40	1.60	1.76

## APPENDIX B: MCMC CORNER PLOTS

We display the corner plots to our best-fitting model ( $\alpha = 0.5$ ) with best-fitting values listed in Table 2. We remove the first 17 500 of 20 000 total steps as burn-in, and plot the posterior distribution. The apparent degeneracy with  $\xi_2$  and  $L_B$  appears in many of the MCMC

fits. This is likely due to some subtleties of the halo model, yet they do not affect the quality of the photometric fits. Because we are primarily interested in constraints on the properties describing the ascent of the leading and trailing screens  $\{\theta_k, \dot{\theta}_k, Y_k, \dot{Y}_k\}$ , to be consistent with Winn et al. (2006), we do not modify the halo model.

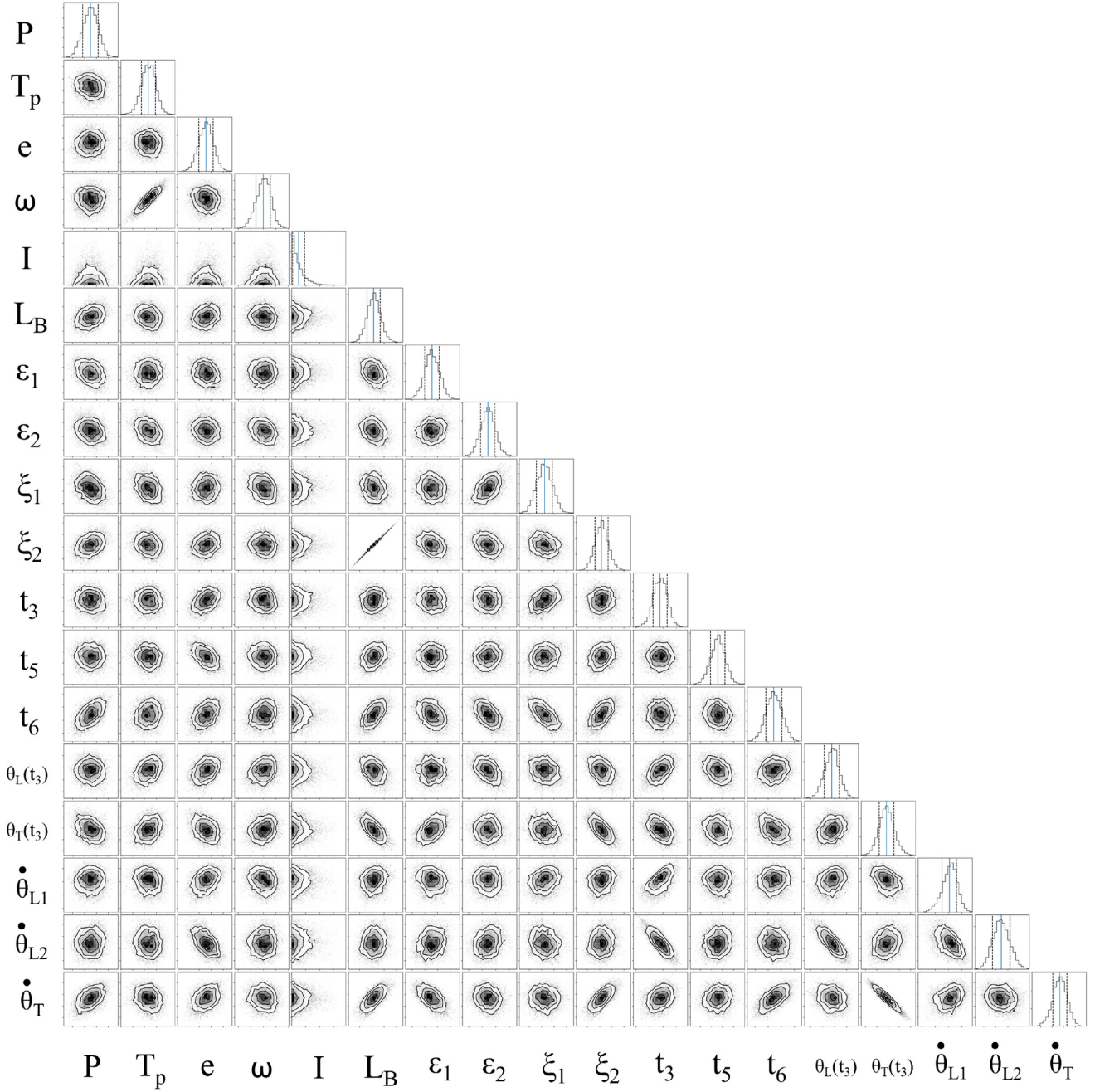


**Figure B1.** Two-dimensional projection of the posterior probability distribution sampled using MCMC for  $\alpha = 0.5$ . Blue solid lines indicate best-fitting values reported in Table 2, whereas black dashed lines indicate a  $1\sigma$  confidence interval.

This paper has been typeset from a  $\text{\LaTeX}$  file prepared by the author.